Electronic Supplementary Information

Interactions Between Water and Rhodium Clusters: Molecular Adsorption versus Cluster Adsorption

Yuhan Jia,[a,b,#] Haiming Wu,[a,#]Xiaoyun Zhao,[c] Hanyu Zhang,[a] Lijun Geng,[a] Hongchao Zhang,[a,b] Sidian Li,[c*] Zhixun Luo[a,b*] and Klavs Hansen[d]

a. Beijing National Laboratory for Molecular Sciences (BNLMS), State Key Laboratory for Structural Chemistry of Unstable and Stable Species, Institute of Chemistry, Chinese Academy of Sciences, Beijing 100190, P. R. China.

b. University of Chinese Academy of Sciences, Beijing 100049, P. R. China

c. Institute of Molecular Science, Shanxi University, Taiyuan 030006, China

d. Center for Joint Quantum Studies and Department of Physics, School of Science, Tianjin University, 92 Weijin Road, Tianjin 300072, China.

* Corresponding Emails: lisidian@sxu.edu.cn (SL); zxluo@iccas.ac.cn (ZL).

Contents

S1. Experimental and computational methods

⬩ Experimental

The formation and interaction of pure and hydrated rhodium clusters are studied by employing a customized reflection time-of-flight mass spectrometer (Re-TOFMS)[1] coupled with an infrared laser system and applying a well-described type of pulsed laser vaporization cluster source (LaVa), together with a compact tube reactor. The Rh_n^+ cluster cations were generated by laser ablation of a rhodium disk in the presence of helium cooling gas released through a pulsed valve with a backing pressure of 10 atm. A pulsed laser (10 Hz 532 nm Nd: YAG) with an average energy of 15-20 mJ/pulse was focused onto the finely polished surface of rhodium disk (ϕ = 16mm, 99.95%) which was installed on a specially designed holder providing rotational and translational motion under motor control. The cluster formation of $Rh_n^{\pm,0}$ in the source waiting room (with a nozzle of ϕ = 1.35 mm) was attained with pulsed buffer gas He (99.999%, 10 bar) controlled by a pulse valve (Parker, Serial 9). Water vapour was injected into the system by the He (99.999%, 1 bar) bubbling method to react with Rh_n^+ in the reaction tube (Φ = 6 mm and length = 60 mm). To supply the reaction tube, another pulse valve was employed to control the amount of injected water. After the reaction, the molecular beam was skimmed (Φ = 2 mm) into a differentially pumped chamber in which the clusters enter the time-of-flight mass spectrometer where they are accelerated perpendicularly to the flow velocity accelerated through five pulsed electrodes and fly through vacuum before entering the reflectron. After exiting from the reflectron, the ions move toward the detector. Here the ions are detected with a dual microchannel plate detector (MCP) and recorded with a digital oscilloscope (Teledyne LeCroy HDO6000).

To get neutral pure and hydrated rhodium clusters, a tangential deflection voltage (DC 200 V) was employed to remove charged ions before skimming. Then, the neutral cluster beam was collimated into the TOF chamber via a ϕ 2 mm skimmer. At the arrival of neutral Rh_n clusters into the ionization zone (i.e., the space between the first and second electrode plates), they meet the counter propagating ionization laser pulse. After ionization by the deep-ultraviolet laser, the neutral clusters were then analyzed by the Re-TOFMS. Considering that the ionization energies of most metal atoms are centered at 7 eV, this Re-TOMFS instrument combined with the 177.3 nm deep-ultraviolet

(DUV) laser will ionize the cluster with one photon.

Infrared photodissociation experiments were performed on the Rh-water compounds. The ion beam from the flow-tube reactor was exposed to radiation of an unfocused 1064 nm laser beam (Continue, Surelite EX) for photodissociation. The used pulse energy was in the range of 30-320 mJ, controlled by adjusting the laser flash voltage. To monitor the photodissociation of $Rh_9^+(H_2O)_3$ and $Rh_8^+(H_2O)_4$ clusters, we collected the mass spectra for a variety of laser pulse energy, and then plotted the relative mass abundances of the fragment ion relative to the parent ion as a function of the laser pulse energy. The uncertainties of relative signal intensities between a pair of spectra were within 5%.

Computational

Ground state structures of the cationic rhodium clusters Rh_n^+ (n=1-9) and related low-lying isomers, as well as the hydrated complexes $Rh_n^+(H_2O)_m$, were optimized utilizing B3LYP hybrid density functional [2-3] within the Gaussian 09 program[4]. We employed the Stuttgart/Dresden SDD effective core potential and basis set [5] for Rh atoms, while 6-311G** [6-7] basis set for O and H atoms. A combination of the functionals and basis sets has been found appropriate in previous studies of cationic rhodium complexes [8-16] and was used here. Vibrational frequency calculations were performed to ensure that the lowest-energy structure of reaction products has no imaginary frequencies, and zero-point vibrational corrections were implemented in all the energy calculations. In each case, several spin configurations were examined to ensure that the lowest energy structure and multiplicity have been identified.

The Vienna Ab initio Simulation Package (VASP) [17] with the projector-augmented wave pseudo-potential (PAW) [18] was also employed to check the cluster structures. For the VASP calculations, long-range electron correlation accounting for van der Waals force was included through a semiempirical dispersion-corrected Becke-Johnson damping function [19-20] (D3-BJ) approach.

Explorations on the quantum theory of atoms in molecules [21] (AIM), localized orbital locator [22] (LOL) analysis, Reduced density gradient [23] (RDG) analysis, natural bond orbital [24] (NBO) analysis and noncovalent interaction plots based on independent gradient model (IGM) were carried out using NBO 6.0 program [25] and Multiwfn software [26] respectively, then visualized with the VMD package [27]. Energy

decomposition analysis-natural orbitals for chemical valence (EDA-NOCV) method and charged decomposition analysis (CDA) [28] were also utilized to study the extent of charge transfer between two fragments.

In addition, natural population analysis (NPA) and analysis of complementary electrostatic surface potential[29] (ESP) were performed to describe the various interactions especially the noncovalent bonding between rhodium clusters and H_2O accurately. Poisson's equation relates the electronic density to the electrostatic potential, $V(r)$, that is created by nuclei and electrons of the system [30]:

$$\nabla^2 V(r) = 4\pi\rho_{(r)} - 4\pi \sum_A Z_A \delta(r - R_A) \qquad (1)$$

Z_A is the charge on nucleus A, located at R_A. Each nucleus and electrons contribute to $V(r)$ and both two terms in the formula must be written by integration, which is simply an expression of Coulomb's law [31]:

$$V(r) = \frac{1}{4\pi\varepsilon_0}\left[\sum_A \frac{Z_A e}{|R_A - r|} - e \int \frac{\rho(r')dr'}{|r' - r|}\right] \qquad (2)$$

Equation (2) is the formula for the ESP, $V(r)$ at the point r. $Z_A e$ represents the charge on nucleus A which located at R_A while $\rho(r')dr'$ is the electronic charge contributions from the distance between r' to r. It is worth noting that it has become customary to express $V(r)$ in units of energy rather than energy/charge although the original definition of $V(r)$ comes from the formula: $V(r) = \Delta E / Q$.
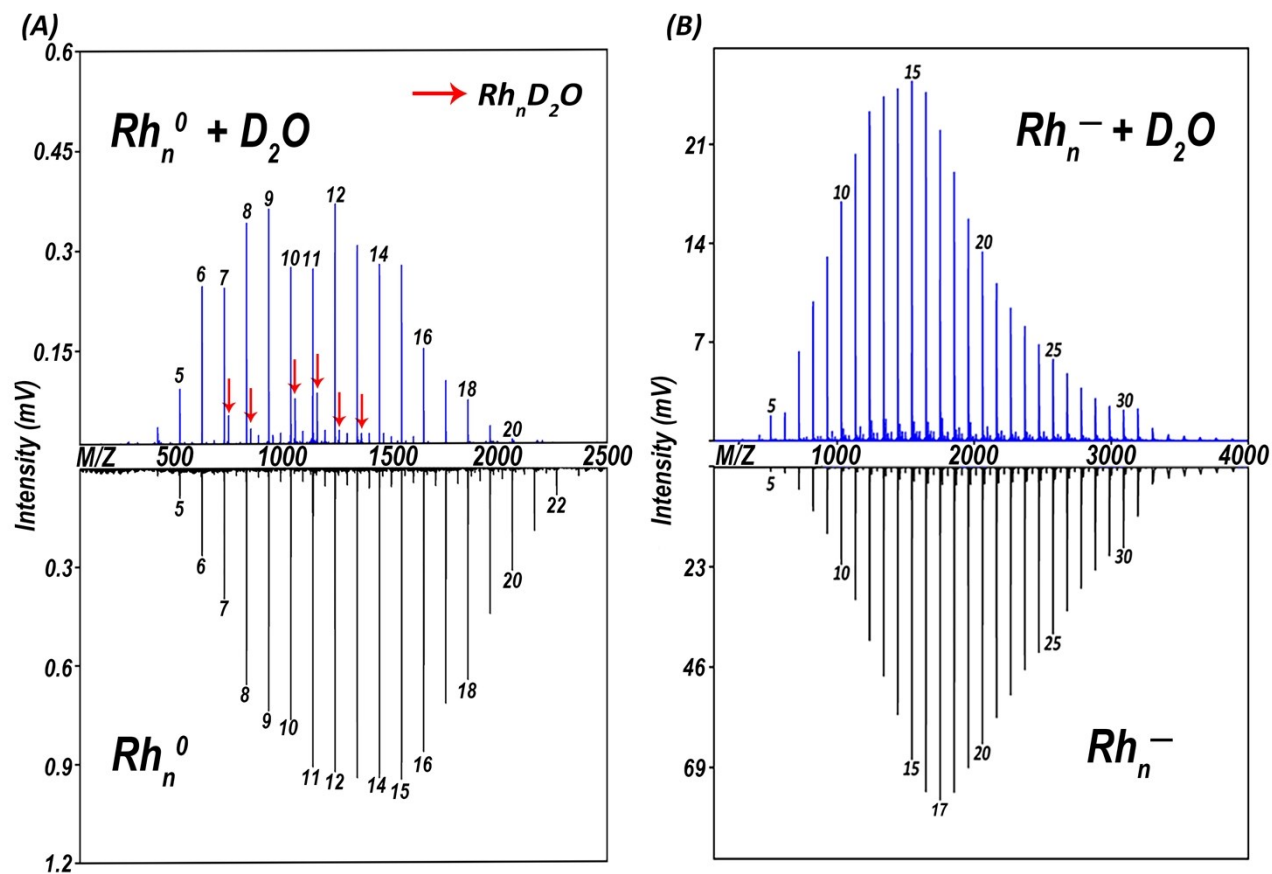
S2. Mass spectrometry observation

Figure S1. Mass spectra of (A) neutral and (B) anionic rhodium cluster produced through LaVa source (below) and after exposure to large quantities of D_2O gas (partial pressure at 150 mPa, above).
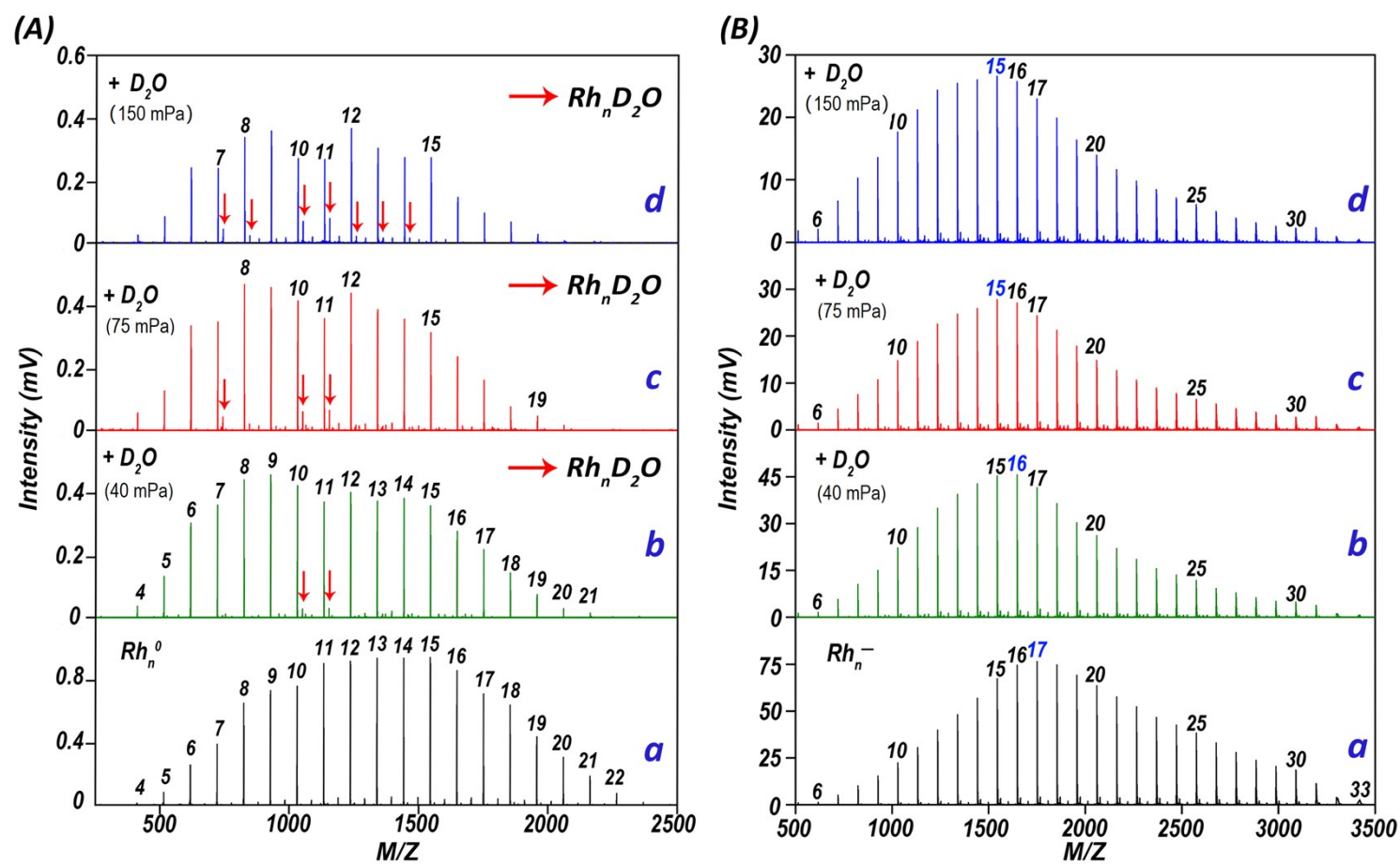
Figure S2. Mass spectra of (A) neutral and (B) anionic rhodium cluster produced through LaVa source after exposure to (b) a small amount of D_2O (partial pressure at ~40 mPa), (c) medium amount of D_2O (partial pressure at ~75 mPa) and (d) large amount of D_2O (partial pressure at ~150 mPa).

Figure S3. Three-dimensional histograms of the integral signal intensities of the observed typical $Rh_8^+(D_2O)_4$ and $Rh_9^+(D_2O)_3$ clusters corresponding to curve C in Fig. 1.
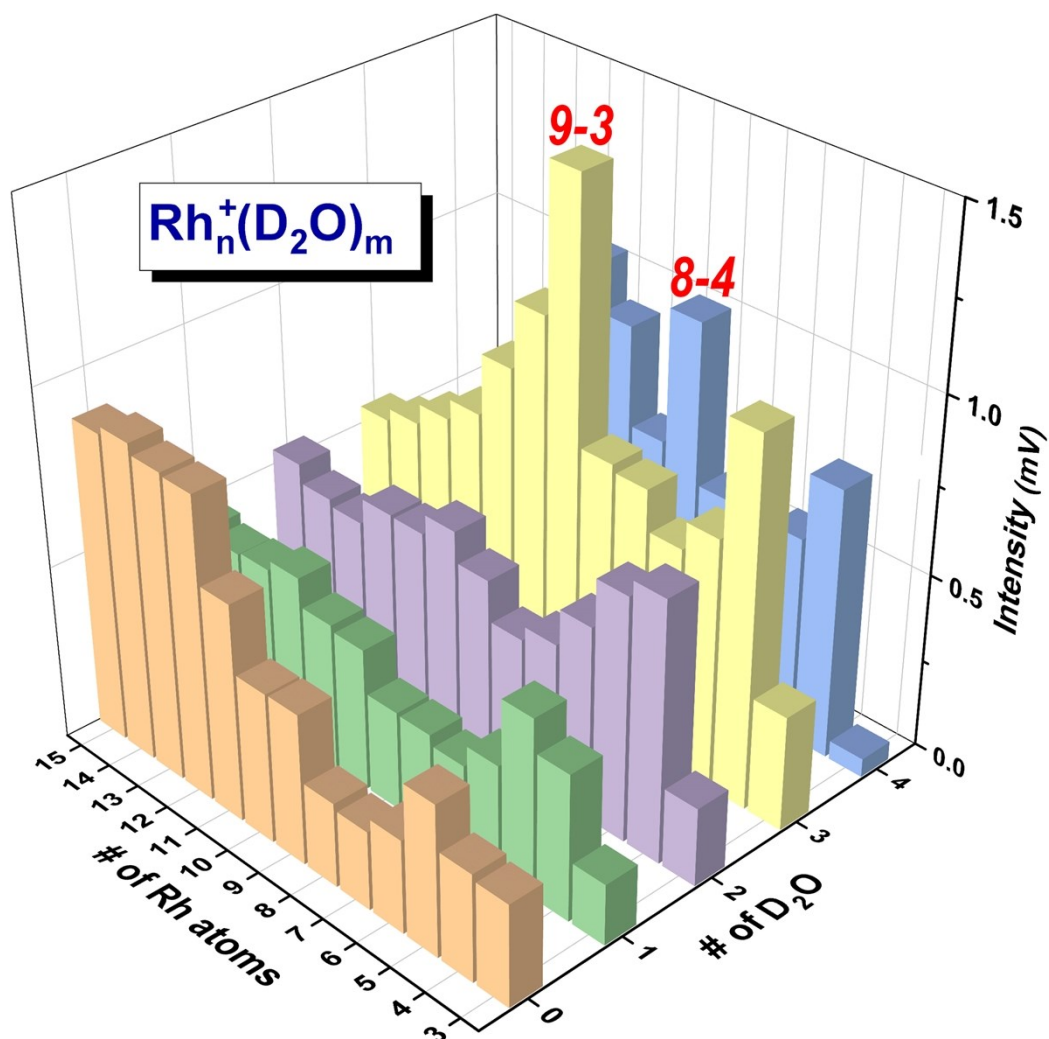
Figure S3 shows the three-dimensional histograms of the integral signal intensities of the observed $Rh_n^+(D_2O)_m$ clusters corresponding to Fig. 1C in the main text. It is clear that $Rh_9^+(D_2O)_3$ is dominant in the case of a moderate amount of vapor.

S3. Repeated experiment with O-18 isotope water
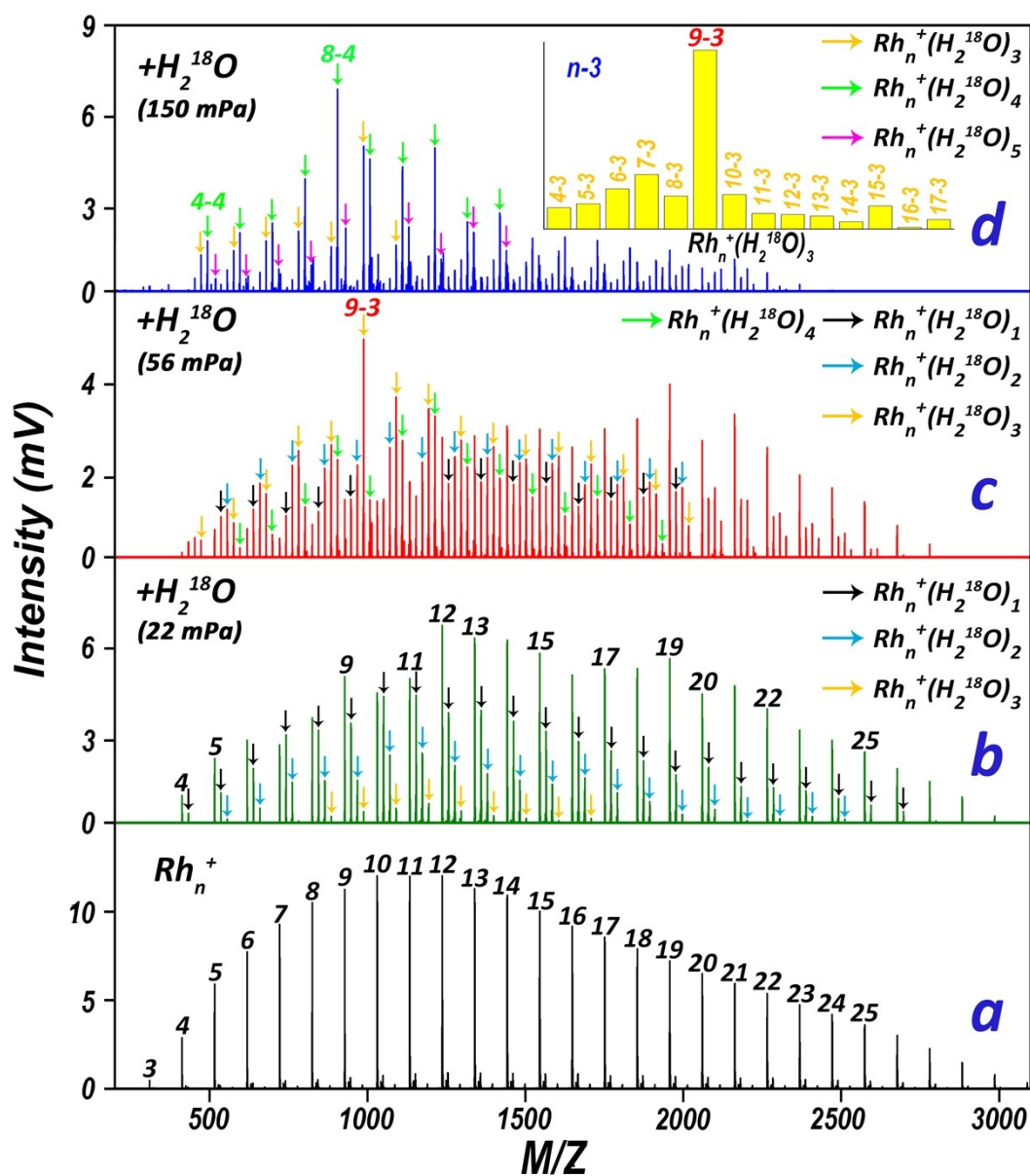
Figure S4. Mass spectra of (a) rhodium cluster cations produced with a LaVa source and after exposure to different amounts of $H_2^{18}O$ vapour provided by helium gas bubbling, with small, medium, large corresponding to pulse value ontime at 100 μs (b), 200 μs (c), 240 μs (d) corresponding to partial pressure at 22 mPa, 56 mPa and 150 mPa respectively). The inset histogram in panel (d) shows the relative intensity of $Rh_n^+(H_2^{18}O)_3$.
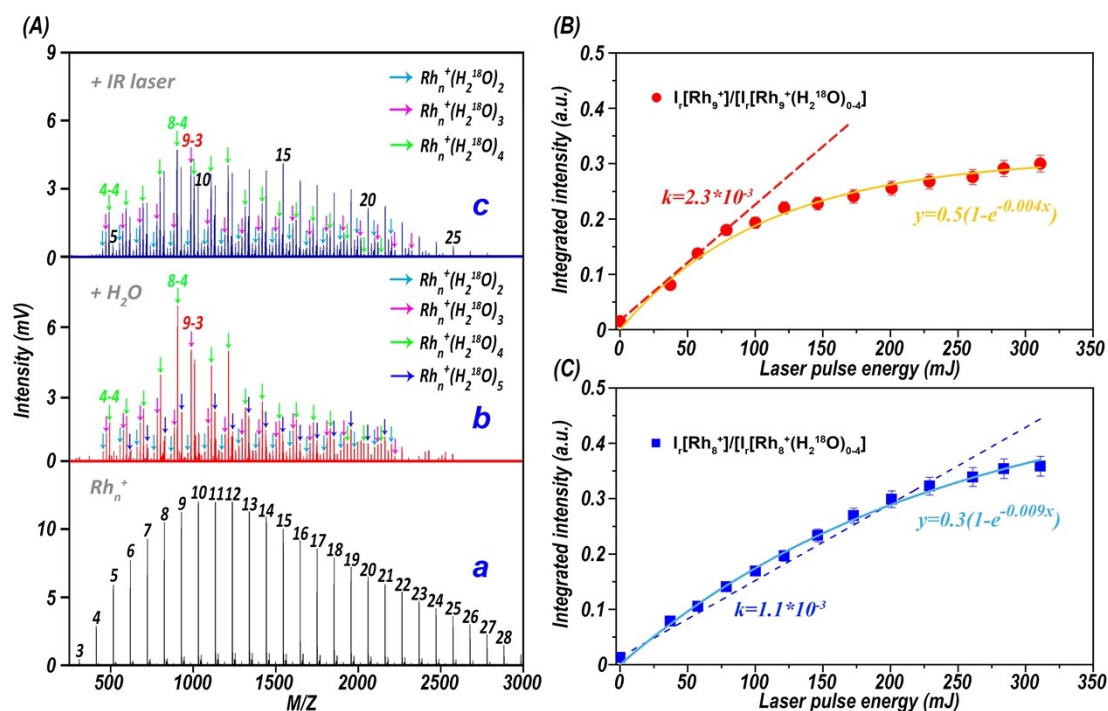
S4. Photodissociation experiment

Figure S5. (A) Mass spectra of Rh_n^+ (a), $Rh_n^+(H_2^{18}O)_m$ (b) produced by the reaction between Rh_n^+ and a large amount of $H_2^{18}O$ (123 mPa) and after exposure to infrared pulsed laser at 311 mJ (c) of the unfocused beam (Φ 6mm), indicating the relative stability of $Rh_8^+(H_2^{18}O)_4$, $Rh_9^+(H_2^{18}O)_3$ as the existence of IR pulsed laser. **(B/C)** integrated intensities of Rh_9^+ and Rh_8^+ relative to the sum of $Rh_9^+(H_2^{18}O)_m$ (m=0-4) and $Rh_8^+(H_2^{18}O)_m$ (m=0-4) respectively, as a function of the 1064-nm laser pulse energy, along with the linear and exponential fitting curves.

We have employed an infrared laser to further examine the stability of these clusters in suffering from likely photodissociation. Figure S5A shows the mass spectra of Rh_n^+ clusters in the absence and presence of $H_2^{18}O$ reactant and the 1064-nm laser radiation. It was found that the exposure to the laser pulse reduces the absolute intensities of $Rh_9^+(H_2O)_3$ and $Rh_8^+(H_2O)_4$, while increases the mass abundances of Rh_9^+ and Rh_8^+. However, the rate of increase of Rh_9^+ and Rh_8^+ is different (Figure S5B and 5C), and both show only a small yield of clusters complexed with 2-4 water molecules (nearly all the $Rh_9^+(H_2O)_5$ series disappear in the presence of strong IR laser).

Figure S5B and 5C plot the integrated intensities of Rh_8^+ and Rh_9^+ relative to $Rh_8^+(H_2O)_m$ and $Rh_9^+(H_2O)_m$ respectively, as a function of the pulse energy of the IR laser. As is shown, the main difference between the two sets of yields is

that the increasing intensity of Rh_8^+ can be fitted with a straight line (a slope $k = 0.011$), whereas Rh_9^+ shows a fast-increasing tendency (a slope $k = 0.023$) at 0~100 mJ and then a relatively slower increasing tendency in parallel to Rh_8^+. This is consistent with the bonding of the four water molecules to the octamer (as individual molecules) while the water in a cyclic $(H_2O)_3$ trimer on the nonamer. It is worth mentioning that the photodissociation of these hydrated Rh clusters at 1064 nm could involve a non-radiative relaxation after photon absorption, and a subsequent unimolecular decay of the thermalized species.

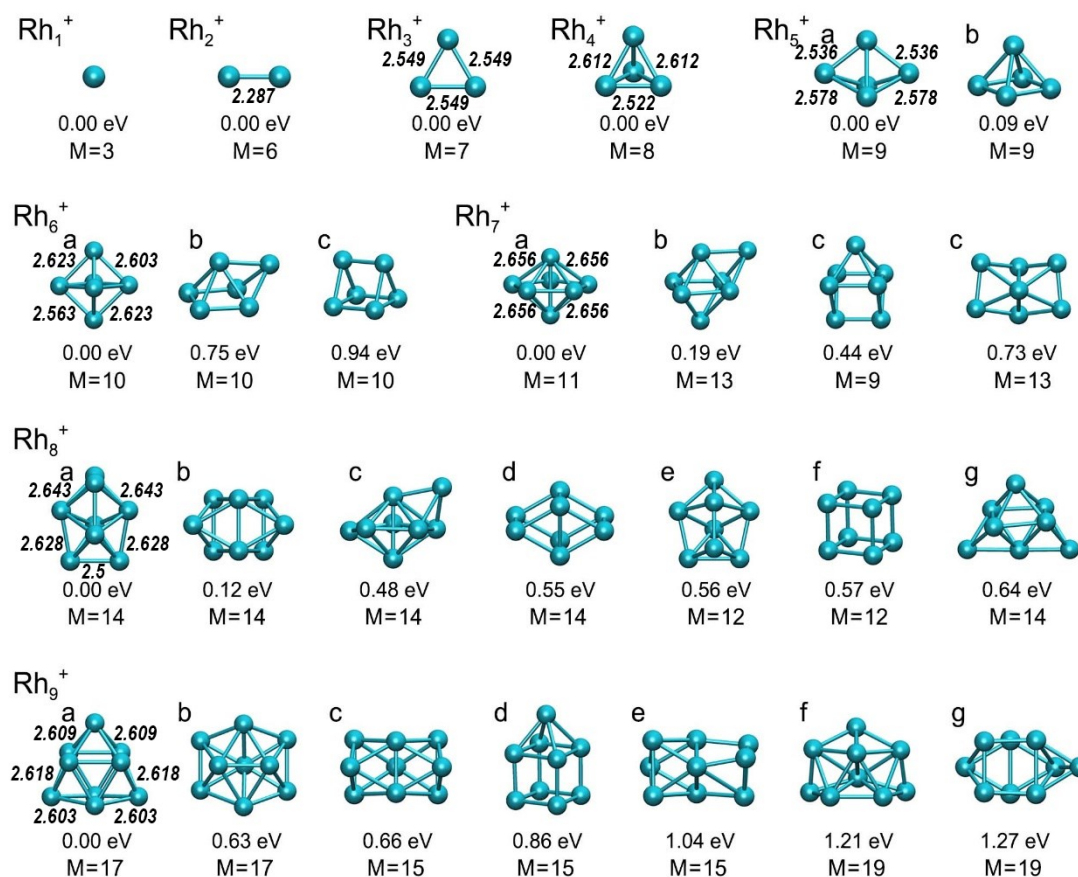# S5. Geometric structures

Figure S6. Isomers of Rh_n^+ (n=1-9) clusters under different spin multiplicities and their relative energy obtained *via* first-principles calculations at the B3LYP-D3/SDD level of theory. The energies and bond lengths are given in eV and angstrom (black), respectively.

Figure S7. Isomers of $Rh_n^+(H_2O)$ (n=1-9) clusters under different spin multiplicities and their relative energy obtained *via* first-principles calculations at the B3LYP-D3/SDD level of theory for element Rh and B3LYP-D3/6-311G** for elements (O, H). The energies and bond lengths are given in eV and angstrom (black), respectively.
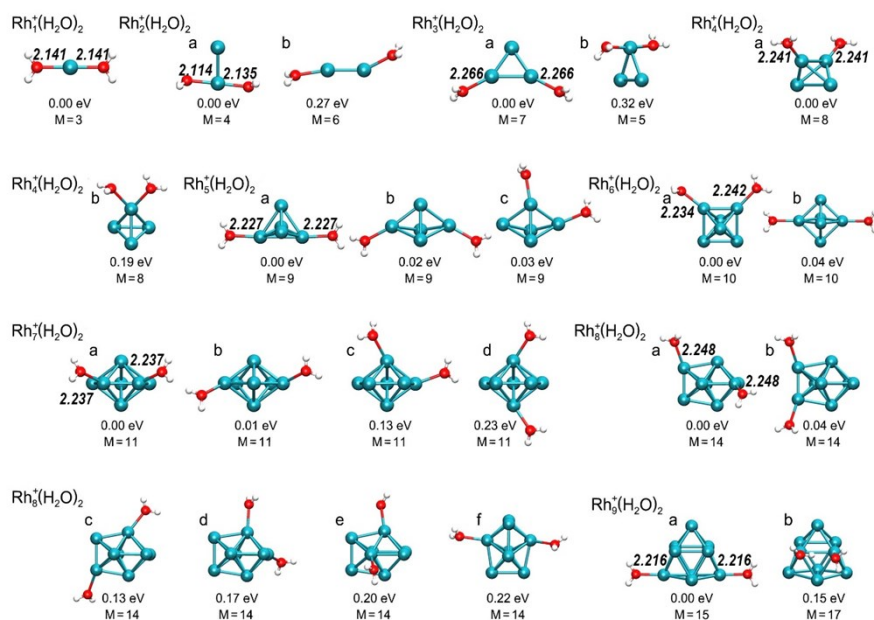
Figure S8. Isomers of $Rh_n^+(H_2O)_2$ (n=1-9) clusters under different spin multiplicities and their relative energy obtained *via* first-principles calculations at the B3LYP-D3/SDD level of theory for element Rh and B3LYP-D3/6-311G** for elements (O, H). The energies and bond lengths are given in eV and angstrom (black), respectively.
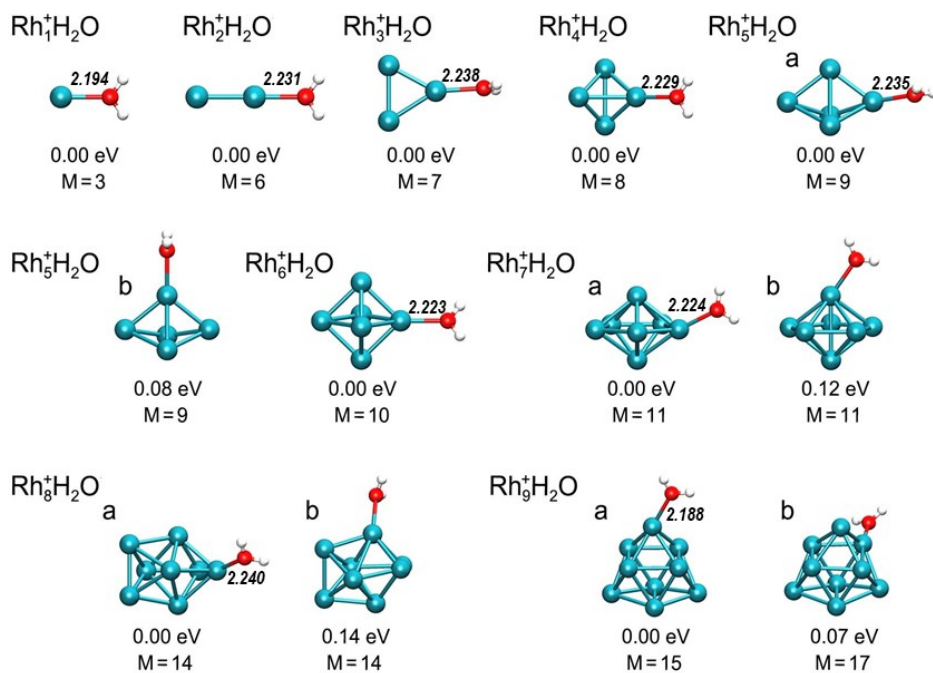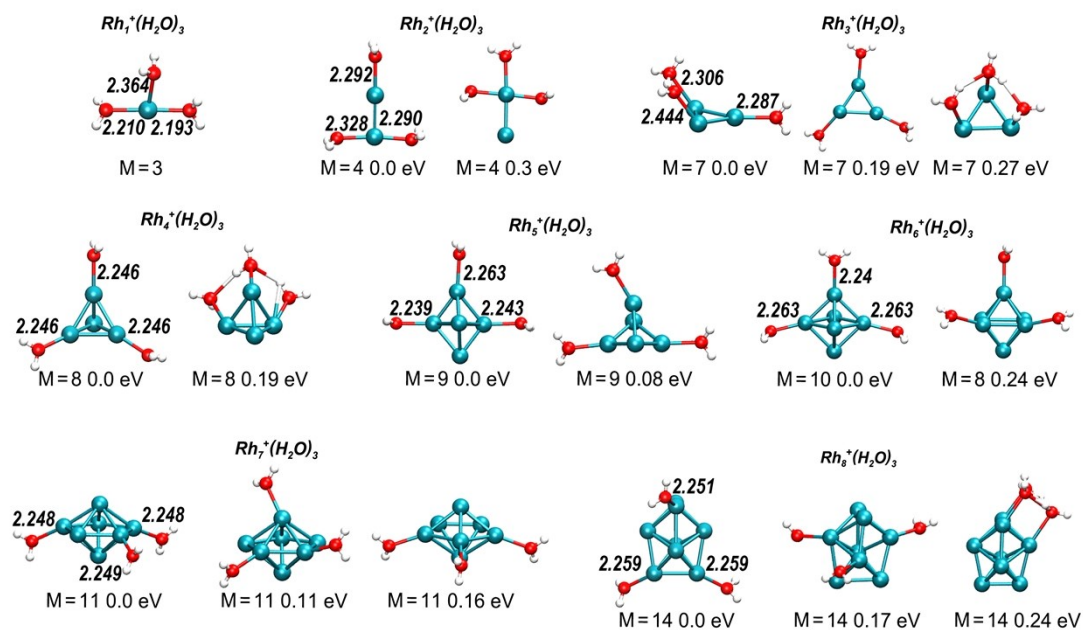
Figure S9. Isomers of $Rh_n^+(H_2O)_3$ (n=1-8) clusters under different spin multiplicities and their relative energy obtained *via* first-principles calculations at B3LYP-D3 functionals and SDD basis sets for element Rh and 6-311G** for elements (O, H). The energies and bond lengths are given in eV and angstrom (black), respectively.

B3LYP-D3/SDD $Rh_9^+(H_2O)_3$
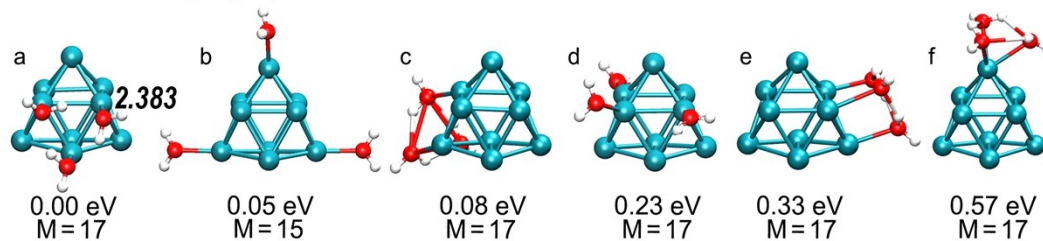
PBE0-D3/SDD $Rh_9^+(H_2O)_3$
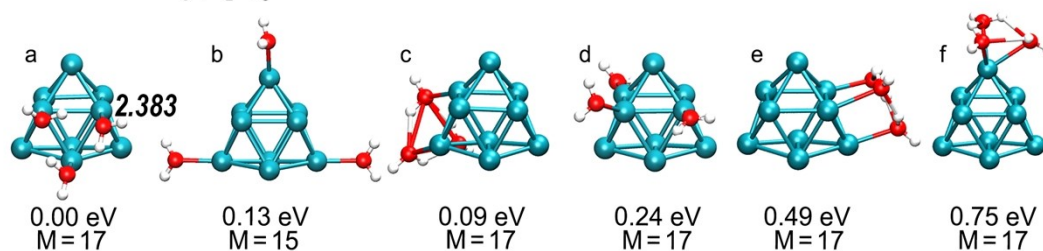
Figure S10. Isomers of $Rh_9^+(H_2O)_3$ clusters under different spin multiplicities and their relative energy obtained *via* first-principles calculations at both B3LYP-D3 and PBE0-D3 functionals and SDD basis sets for element Rh and 6-311G** for elements (O, H). The energies and bond lengths are given in eV and angstrom (black), respectively.
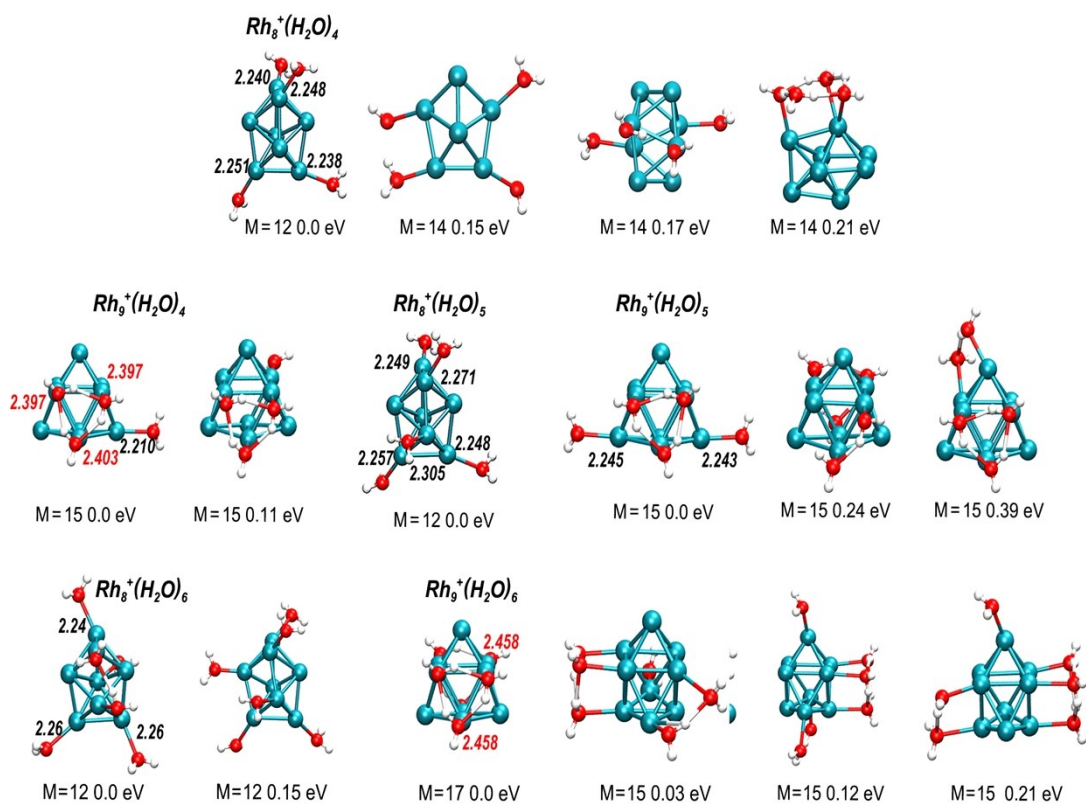
Figure S11. Optimized structures of the other $Rh_{8,9}^+(H_2O)_m$ (m=4-6) clusters *via* first-principles calculations at both B3LYP-D3 SDD basis sets for element Rh and 6-311G** for elements (O, H). The energies and bond lengths are given in eV and angstrom (black), respectively.

To further explore the stability of a water trimer on Rh_9^+ cluster, we have employed the Vienna Ab-initio Simulation Package (VASP)[17] to optimize the structure of the $Rh_9(H_2O)_3$ isomers. The interactions are described using the projector-augmented-wave (PAW) method, while the Perdew-Burke-Ernzehof (PBE) functional in the generalized gradient approximation (GGA) was utilized to treat the electronic exchange-correlation energy. As shown in Figure S12A. and B, the $(H_2O)_3$ water trimer on Rh_9 shows lower energy than that of three isolated water molecules, which is consistent with that obtained by Gaussian optimization. Note that the structure of $(H_2O)_3$ water trimer on Rh(111) surface finds lower energy than three neighboring water molecules adsorbed on the Rh(111) surface, as shown in Figure S12D. versus E. A further visualization is shown by the simulated STM image (Figure S12F) of a few $(H_2O)_3$ water clusters on the Rh(111)-surface generated by using the P4VASP package, with a continuously varying scanning distance.
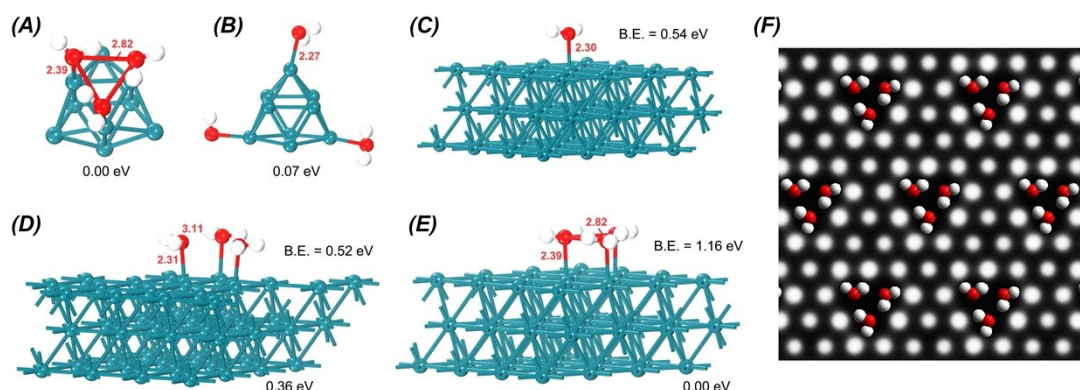
Figure S12. **(A-B)** The VASP-optimized neutral structures of $Rh_9(H_2O)_3$ isomers, showing the same energy minima structure as that obtained by Gaussian optimization. **(C)** A single H_2O molecule on Rh(111) surface, in a comparison with three isolated H_2O molecules **(D)** and a water trimer **(E)** on the Rh(111) surface. **(F)** The simulated STM image of Rh(111)-supported $(H_2O)_3$ clusters. All the energies are given in eV (1 eV = 23.06 kcal/mol).
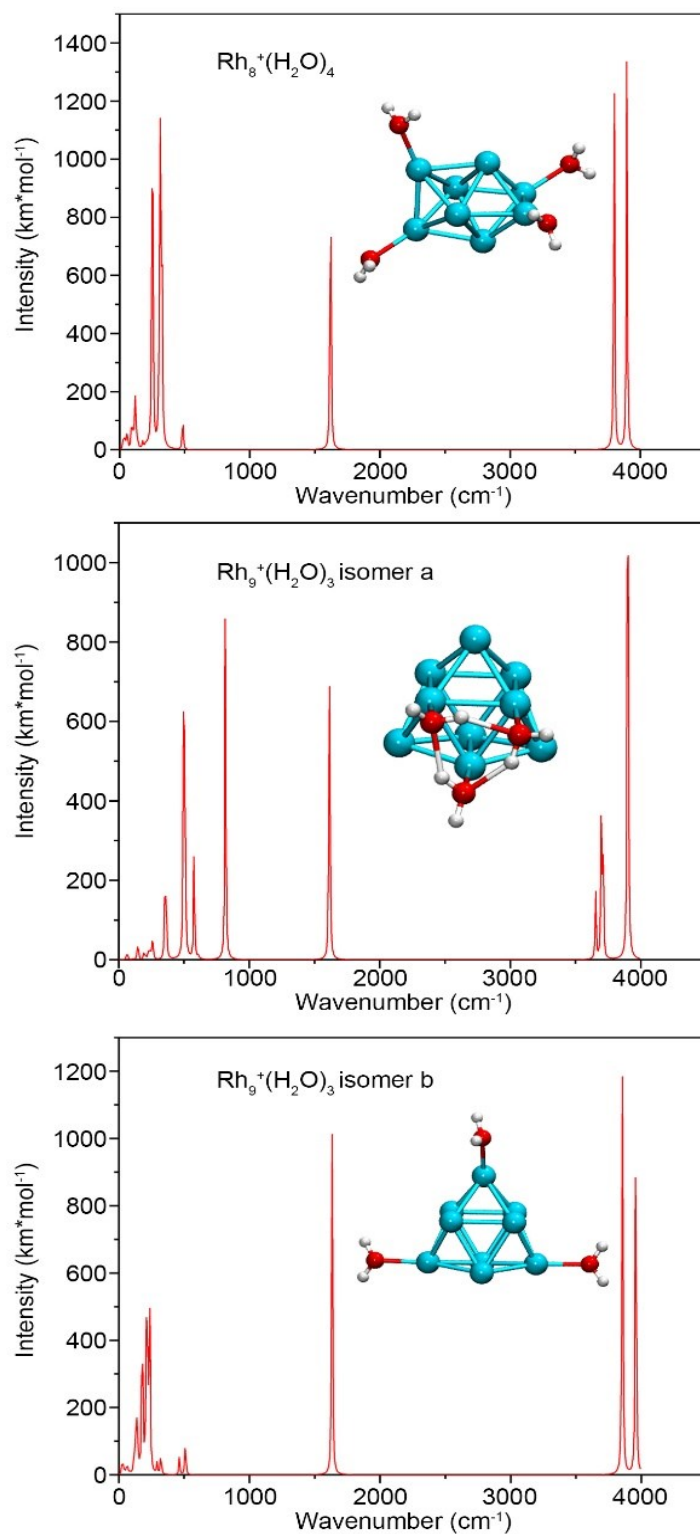
Figure S13. The simulated infrared spectrum of $Rh_8^+(H_2O)_4$ and $Rh_9^+(H_2O)_3$ (both isomers a and b).

S6. Energetics

Table S1. Electronic affinity (i.e., ionization energy of the neutral), formation energy defined by "$E(Rh_{n-1}^+) + E(Rh) - E(Rh_n^+)$" and HOMO-LUMO gap of the Rh_n^+ (n=2-9) clusters. All the energies are given in eV (1 eV = 23.06 kcal/mol).

	HOMO-LUMO gap	Electron affinity	Formation energy
Rh_2^+	3.99	7.47	0.99
Rh_3^+	4.15	6.86	1.69
Rh_4^+	3.86	6.21	2.13
Rh_5^+	2.83	5.79	2.30
Rh_6^+	2.34	5.69	2.49
Rh_7^+	2.04	5.31	2.54
Rh_8^+	1.39	5.94	2.63
Rh_9^+	1.37	6.19	2.70
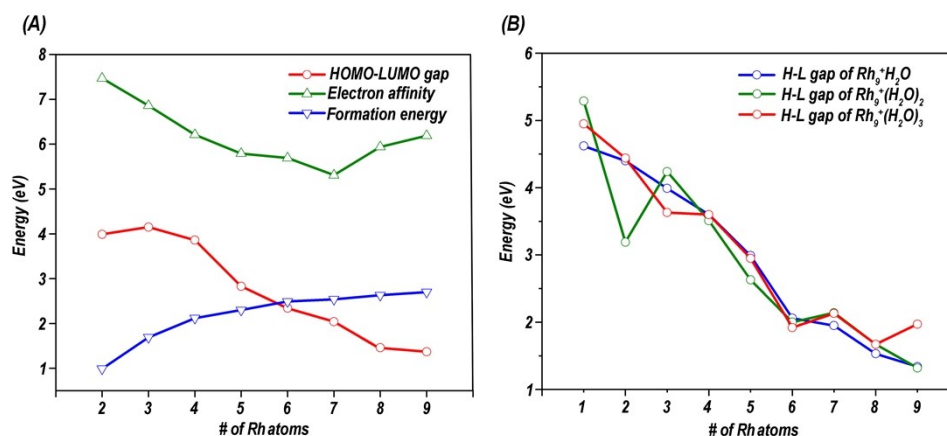
Figure S14. (A) HOMO-LUMO gap (red), electronic affinity (green) and formation energy (blue) of Rh_n^+(n=2-9); (B)HOMO-LUMO gap of $Rh_n^+(H_2O)_m$ (n=1-9, m=1-3).

Table S2. Relative energy of both global minima (a) of $Rh_9^+(H_2O)_3$ and its competing isomer (b) obtained via first-principles calculations at multiple functionals and basis sets.

Functional /basis set	SDD		LANL2DZ	
	a	**b**	**a**	**b**
B3LYP-D3	**0.00**	0.05	**0.00**	0.05
PBE0-D3	**0.00**	0.13	**0.00**	0.10
TPSS-D3	**0.00**	0.24	**0.00**	0.14
BP86-D3	**0.00**	0.32	**0.00**	0.21

Table S3. Thermodynamic energy of Rh_n^+ isomers under different spin multiplicities obtained via first-principles calculations at the B3LYP-D3/SDD level of theory (eV).

Rh_n^+		Energy			
n=1		M=1	M=3	M=5	M=7
		2.07	**0.00**	2.23	11.41
n=3		M=5	M=7	M=9	M=11
		0.33	**0.00**	1.80	4.63
n=5		M=5	M=7	M=9	M=11	M=13
	a	0.37	1.09	**0.00**	1.02	2.29
	b	0.66	0.76	0.09	1.30	2.20
n=7		M=7	M=9	M=11	M=13	M=15
	a		0.59	**0.00**	0.22	0.71
	b	0.77	0.58	0.44	0.19	0.80
	c	0.72	0.44	0.73	0.49	0.54
	d		1.22	1.03	0.73	1.33
n=9		M=13	M=15	M=17	M=19	M=21
	a	0.59	0.31	**0.00**	0.27	
	b	0.85	1.18	0.63	1.13	
	c	0.89	0.66	1.34	1.18	
	d	0.93	0.86	1.19	1.04	
	e	1.39	1.04	1.53	1.23	
	f	1.70	1.53	1.49	1.21	2.50
	g	1.33	1.71	1.81	1.27	2.78

Rh_n^+		Energy			
n=2		M=2	M=4	M=6	M=8
		1.04	0.44	**0.00**	3.36
n=4		M=4	M=6	M=8	M=10
		0.85	0.64	**0.00**	1.24
n=6		M=8	M=10	M=12	
	a	0.94	**0.00**	0.76	
	b	1.15	0.75	0.76	
	c	1.10	0.94	1.32	
n=8		M=10	M=12	M=14	M=16
	a	0.61	0.18	**0.00**	0.36
	b	0.58	0.33	0.12	0.48
	c		0.86	0.48	0.67
	d	1.56	0.95	0.55	0.83
	e	0.91	0.56	0.83	1.09
	f	1.26	0.57	0.71	0.85
	g		1.23	0.64	0.76

Table S4. Thermodynamic energy of $Rh_n^+(H_2O)$ isomers under different spin multiplicities obtained via first-principles calculations at the B3LYP-D3/SDD level of theory for element Rh and B3LYP-D3/6-311G** for elements (O, H) (eV).

Left half:

$Rh_n^+H_2O$		Energy		
n=1		M=1	M=3	M=5
		1.99	**0.00**	2.04
n=3		M=5	M=7	M=9
		0.53	**0.00**	1.90
n=5		M=7	M=9	M=11
	a	0.41	**0.00**	1.02
	b	0.42	0.08	0.77
n=7		M=9	M=11	M=13
	a	0.52	**0.00**	0.33
	b	0.68	0.12	0.25

Right half:

$Rh_n^+H_2O$		Energy			
n=2		M=4	M=6	M=8	
		0.41	**0.00**	2.83	
n=4		M=6	M=8	M=10	
		0.37	**0.00**	1.52	
n=6		M=8	M=10	M=12	
		0.12	**0.00**	0.66	
n=8		M=12	M=14	M=16	
	a	0.17	**0.00**	0.36	
	b	0.32	0.14	0.39	
n=9		M=13	M=15	M=17	M=19
	a	0.48	**0.00**	0.15	0.45
	b	0.64	0.18	0.07	0.44

Table S5. Thermodynamic energy of $Rh_n^+(H_2O)_2$ isomers under different spin multiplicities obtained via first-principles calculations at the B3LYP-D3/SDD level of theory for element Rh and B3LYP-D3/6-311G** for elements (O, H) (eV).

$Rh_n^+(H_2O)_2$		Energy			
n=1		M=1	M=3	M=5	
		0.76	**0.00**	2.45	
		M=3	M=5	M=7	M=9
n=3	a		0.52	**0.00**	1.93
	b	0.41	0.32	0.35	2.08
		M=7	M=9	M=11	
n=5	a	0.40	**0.00**	0.75	
	b	0.31	0.02	0.66	
	c	0.35	0.03	0.90	
		M=9	M=11	M=13	
	a	0.51	**0.00**	0.19	
n=7	b	0.51	0.01	0.12	
	c	0.69	0.13	0.21	
	d	0.69	0.23	0.33	
		M=13	M=15	M=17	M=19
n=9	a	0.49	**0.00**	0.27	
	b	0.77	0.49	0.15	0.76

$Rh_n^+(H_2O)_2$		Energy			
		M=2	M=4	M=6	M=8
n=2	a	0.37	**0.00**	0.27	3.14
	b		0.46	0.27	3.14
		M=6	M=8	M=10	
n=4	a	0.32	**0.00**	1.15	
	b	0.38	0.19	1.34	
		M=8	M=10	M=12	
n=6	a	0.22	**0.00**	0.59	
	b	0.19	0.04	0.67	
		M=12	M=14	M=16	
	a	0.13	**0.00**	0.45	
	b	0.13	0.04	0.37	
n=8	c	0.31	0.13	0.35	
	d	0.26	0.17	0.48	
	e	0.42	0.20	0.44	
	f	0.42	0.22	0.38	

Table S6. Thermodynamic energy of $Rh_n^+(H_2O)_3$ isomers under different spin multiplicities obtained via first-principles calculations at the B3LYP-D3/SDD level of theory for element Rh and B3LYP-D3/6-311G** for elements (O, H).

$Rh_n^+(H_2O)_3$		Energy (eV)	
n=1		M=1	M=3
		0.60	**0.00**
n=2		M=4	M=6
		0.29	**0.00**
n=3		M=5	M=7
		0.48	**0.00**
n=4		M=6	M=8
		0.22	**0.00**
n=5		M=7	M=9
		0.36	**0.00**
n=6		M=8	M=10
		0.24	**0.00**
n=7		M=9	M=11
	a	0.44	0.03
	b	0.47	**0.00**
	c	0.50	0.12
n=8		M=12	M=14
	a	0.08	**0.00**
	b	0.43	0.17
n=9		M=15	M=17
	a	0.36	**0.00**
	b	0.05	0.32
	c	0.32	0.23

Table S7. Thermodynamic energy of $Rh_n^+(H_2O)_4$ isomers under different spin multiplicities obtained via first-principles calculations at the B3LYP-D3/SDD level of theory for element Rh and B3LYP-D3/6-311G** for elements (O, H).

$Rh_n^+(H_2O)_4$		Energy (eV)			
n=1		M=1	M=3	M=5	
		0.60	**0.00**	2.49	
n=4		M=6	M=8	M=10	
		0.22	**0.00**	1.34	
		M=10	M=12	M=14	M=16
n=8	a	0.41	**0.00**	0.05	
	b		0.18	0.15	0.32
	c		0.59	0.17	0.48

Table S8. Thermodynamic energy of $Rh_n^+(H_2O)_3$ and $Rh_n^+(H_2O)_4$ isomers under different spin multiplicities obtained via first-principles calculations at the B3LYP-D3/LANL2TZf level of theory for element Rh and B3LYP-D3/6-311G** for elements (O, H).

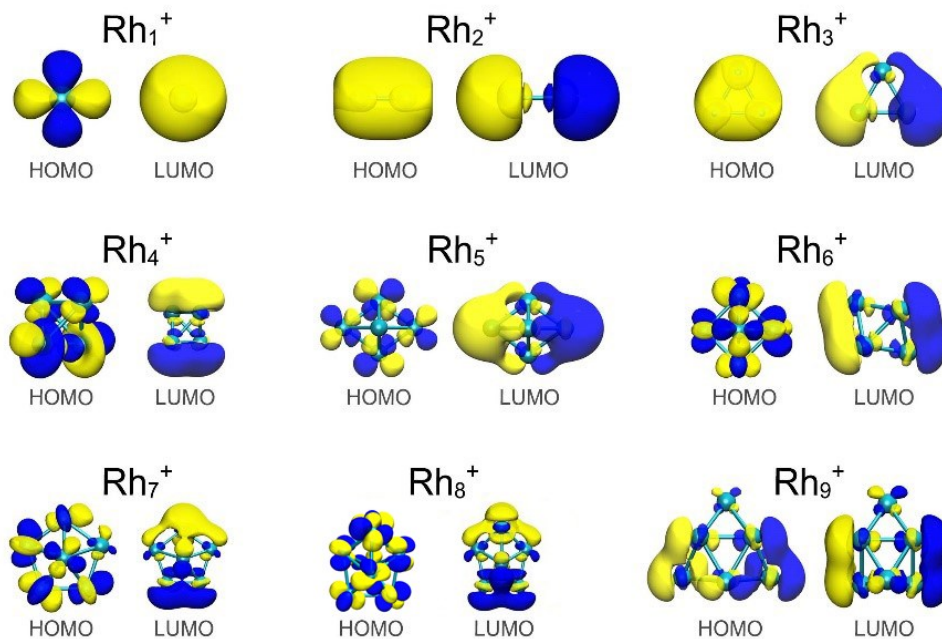| $Rh_n^+(H_2O)_3$		Energy (eV)				$Rh_n^+(H_2O)_4$		Energy (eV)			
		M=13	M=15	M=17	M=19			M=10	M=12	M=14	M=16
n=9	a	/	0.22	0.00	0.89	n=8	a	0.46	**0.00**	0.14	/
	b	0.28	0.06	0.38	/		b	0.55	0.10	0.19	/
	c	/	0.27	0.16	0.92		c	/	0.64	0.25	0.53

S7. Frontier orbitals

Figure S15. Frontier molecular orbitals of Rh_n^+ (n<10) clusters obtained *via* first-principles calculations at the B3LYP-D3/SDD level of theory.
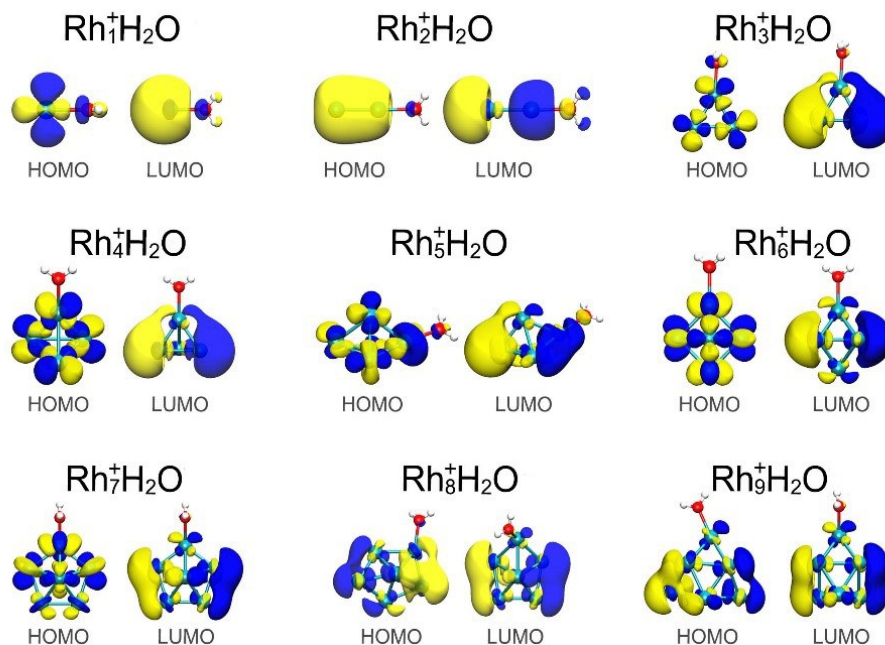

Figure S16. Frontier molecular orbitals of $Rh_n^+H_2O$ (n<10) clusters obtained *via* first-principles calculations at the B3LYP-D3/SDD level of theory for element Rh and B3LYP-D3/6-311G** for elements (O, H).

Figure S17. Frontier molecular orbitals of $Rh_n^+(H_2O)_2$ (n<10) clusters obtained *via* first-principles calculations at the B3LYP-D3/SDD level of theory for element Rh and B3LYP-D3/6-311G** for elements (O, H).
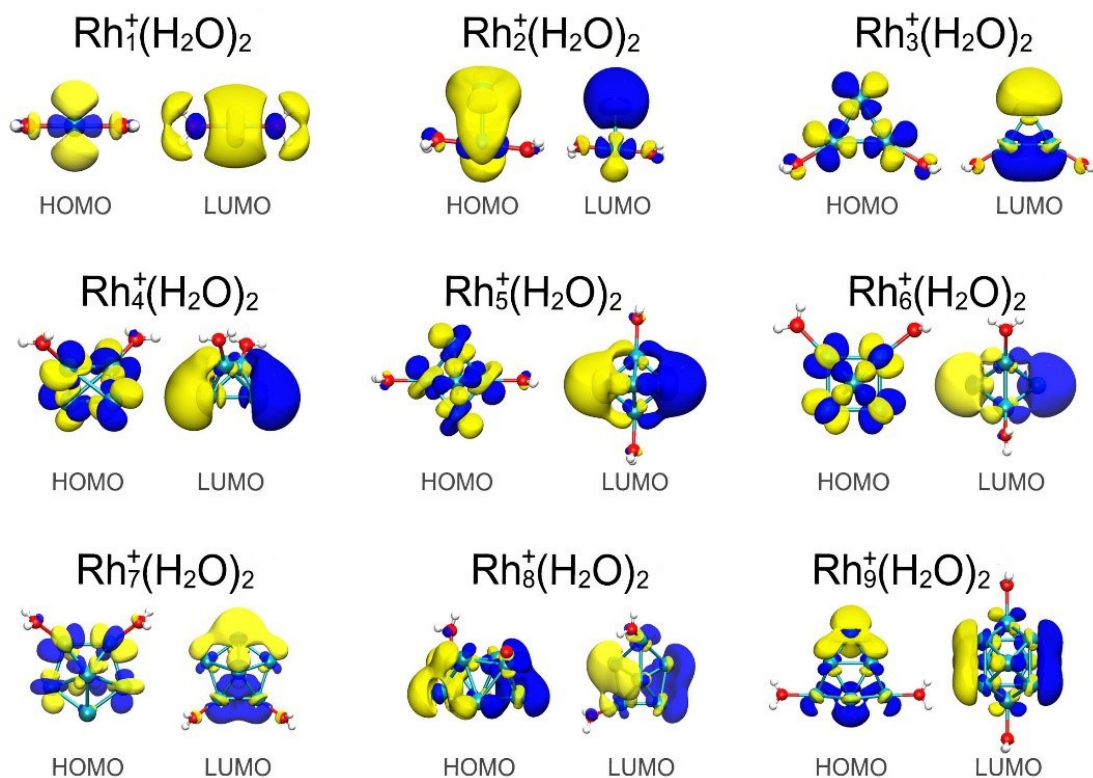
(A)

Rh$_1^+$(H$_2$O)$_3$

HOMO   LUMO

Rh$_2^+$(H$_2$O)$_3$

HOMO   LUMO

Rh$_3^+$(H$_2$O)$_3$

HOMO   LUMO

Rh$_4^+$(H$_2$O)$_3$

HOMO   LUMO

Rh$_5^+$(H$_2$O)$_3$

HOMO   LUMO

Rh$_6^+$(H$_2$O)$_3$

HOMO   LUMO

Rh$_7^+$(H$_2$O)$_3$

HOMO   LUMO

Rh$_8^+$(H$_2$O)$_3$

HOMO   LUMO

Rh$_9^+$(H$_2$O)$_3$

HOMO   LUMO

(B)

Rh$_1^+$(H$_2$O)$_4$

HOMO   LUMO

Rh$_4^+$(H$_2$O)$_4$

HOMO   LUMO

Rh$_8^+$(H$_2$O)$_4$

HOMO   LUMO

Figure S18. Frontier molecular orbitals of (A) Rh$_n^+$(H$_2$O)$_3$ (n=1-9) and (B) Rh$_n^+$(H$_2$O)$_4$ (n=1, 4, 8)clusters obtained *via* first-principles calculations at the B3LYP-D3/SDD level of theory for element Rh and B3LYP-D3/6-311G** for elements (O, H).
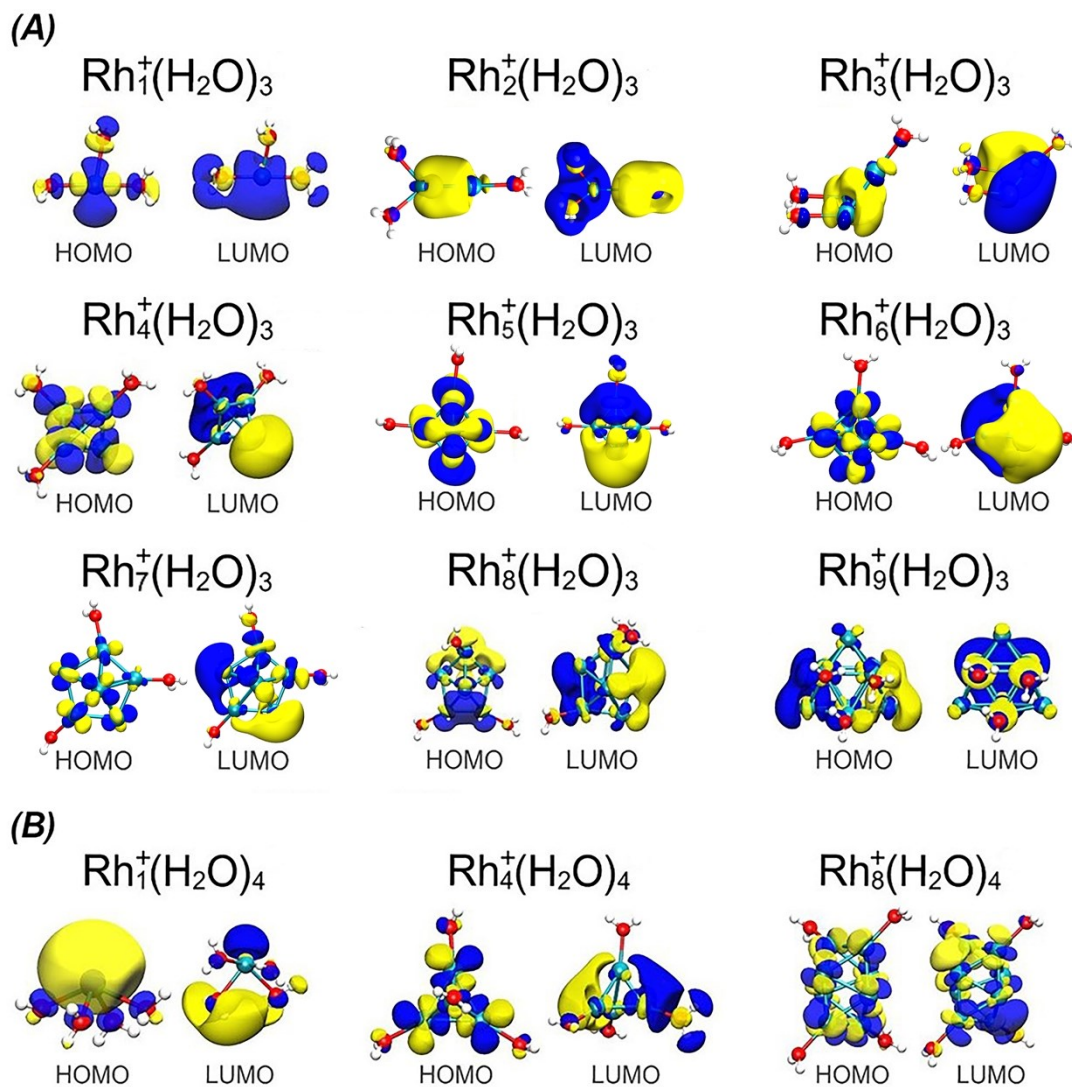
S8. AIM topological analysis

The quantum theory of "atoms in molecules" (AIM) was applied to quantitatively figure out the different interactions of Rh_9^+ with a water trimer $(H_2O)_3$ in comparison to that of Rh_8^+ with four water molecules, as well as the nature of H-bonds in $Rh_9^+(H_2O)_3$ and a free $(H_2O)_3$. Based on the AIM method, we conducted a topological analysis to calculate Rh-O bonding interactions in the $Rh_9^+(H_2O)_3$ and $Rh_8^+(H_2O)_4$ systems. According to the basic topological parameters (Table S12), the electron density ρ represents the bonding strength; and the energy density H(r) determined by the bonding interaction of two atoms enables one to distinguish covalent interaction ($H<0$) or noncovalent bonding ($H>0$) [32]. The symbol H/ρ and indicator $G/-V$ (G: electron kinetic, V: potential) allows a further judgment of the interatomic interactions, i.e., $G/(-V) > 1$ identifies noncovalent bond [33]. In addition, the bond ellipticity indicator ($\varepsilon = \lambda_1/\lambda_2-1$, where λ_1 and λ_2 are the first and the second smallest eigenvalues of the Hessian matrix of the electron density) shows a measure of the degree to which an orbital deviate from the axis of symmetry.

Table S9. Topological parameters of the Rh-O bond critical points (BCP) in $Rh_9^+(H_2O)_3$ and $Rh_8^+(H_2O)_4$ calculated at B3LYP-D3/SDD level of theory for Rh, and B3LYP-D3/6-311G** for elements O and H.

	ρ	$H(r)$	H/ρ	$G/-V$	ε
	0.04276	0.00004	0.00051	1.00042	0.27381
$Rh_9^+(H_2O)_3$	0.04124	0.00007	0.00161	1.00133	0.28132
	0.04248	0.00004	0.00091	1.00074	0.26872
	0.05498	-0.00003	-0.00057	0.99958	0.09913
	0.05591	-0.00008	-0.00142	0.99897	0.06039
$Rh_8^+(H_2O)_4$	0.05551	-0.00013	-0.00229	0.99832	0.08921
	0.05617	-0.00010	-0.00171	0.99876	0.07831

Table S10. Topological parameters of the H-bond critical points (BCP) in $Rh_9^+(H_2O)_3$ and free $(H_2O)_3$ calculated at B3LYP-D3/SDD for Rh, while 6-311G** for O and H.

	ρ	$H(r)$	H/ρ	$G/-V$	ε
	0.02405	0.00227	0.09458	1.12100	0.05525
$Rh_9^+(H_2O)_3$	0.02269	0.00233	0.10280	1.13376	0.05118
	0.02204	0.00233	0.10572	1.13871	0.04959
	0.03162	0.00050	0.01588	1.01925	0.07585
$(H_2O)_3$	0.03171	0.00048	0.01500	1.01816	0.07612
	0.03166	0.00049	0.01533	1.01858	0.07603

S9. Mayer bond order

Table S11. Optimized geometric parameters and Mayer bond order of $Rh_9^+(H_2O)_3$ and $Rh_8^+(H_2O)_4$ clusters at the B3LYP-D3/SDD for Rh, 6-311G** for O, H level of theory.

	Bond	*Mayer bond order*	*Bond length* (Å)
	Rh(1)-O(13)	0.232	2.38
$Rh_9^+(H_2O)_3$	Rh(2)-O(10)	0.234	2.40
	Rh(3)-O(16)	0.229	2.38
	Rh(1)-O(12)	0.374	2.25
$Rh_8^+(H_2O)_4$	Rh(4)-O(18)	0.386	2.24
	Rh(7)-O(9)	0.371	2.25
	Rh(8)-O(15)	0.356	2.24

S10. Energy decomposition analysis (EDA)

We have conducted the energy decomposition analysis based on natural orbitals for chemical valence (EDA-NOCV) method, using Amsterdam Modeling Suits (ADF) program [34]. The EDA, conducted at the B3LYP-D3/TZ2P for element Rh and TZP for elements (O, H) level of theory, divides fragments interaction energy into three parts,

$\Delta E_{int} = \Delta E_{elstat} + \Delta E_{pauli} + \Delta E_{orb}$

where ΔE_{elstat} represents the electrostatic attraction energy, while ΔE_{pauli} is the Pauli repulsion energy; ΔE_{orb} is the attraction energy that results from orbital interaction, as shown in Table S12.

Table S12. EDA-NOCV results for $Rh_9^+(H_2O)_3$ at the B3LYP-D3/TZ2P for element Rh and TZP for elements (O, H) level of theory using the EDA method by ADF program, regarding $(H_2O)_3$ fragments in singlet while Rh_9^+ in 17-et as interacting fragments.

Energy term	Assignment	Interaction Fragments
		$Rh_9^+ + (H_2O)_3$
ΔE_{int}		-36.94
ΔE_{elstat}		**-99.39 (33.13 per water)**
ΔE_{pauli}		110.64
ΔE_{disp}		-8.80
ΔE_{orb}		-39.38
$\Delta E_{orb(1)[\alpha]}$	$(H_2O)_3$ (HOMO-1)→Rh_9^+ (LUMO) donation	-6.14 (15.7%)
$\Delta E_{orb(1)[\beta]}$	$(H_2O)_3$ (HOMO)→Rh_9^+ (LUMO+5) donation	-8.38 (21.5%)
$\Delta E_{orb(2)[\alpha]}$	$(H_2O)_3$ (HOMO)→Rh_9^+ (LUMO+8) donation	-6.56 (16.8%)
$\Delta E_{orb(2)[\beta]}$	$(H_2O)_3$ (HOMO-1)→Rh_9^+ (LUMO+2) donation	-5.19 (13.3%)
$\Delta E_{orb(3)[\beta]}$	**$(H_2O)_3$ polarization**	**-6.85 (17.6%)**
$\Delta E_{orb(rest)[\alpha + \beta]}$		-6.13 (15.7%)

Note: ΔE_{elstat}, electrostatic interaction energy; ΔE_{pauli}, Pauli repulsion energy; ΔE_{orb}, orbital interaction energy; ΔE_{disp}, dispersion energy; ΔE_{int}, total interaction energy. All energies are given in Kcal/mol.

Table S13. EDA-NOCV results for $Rh_8^+(H_2O)_4$ at the B3LYP-D3/TZ2P for element Rh and TZP for elements (O, H) level of theory using the EDA method by ADF program, regarding $4H_2O$ fragments in singlet while Rh_8^+ in 14-et as interacting fragments.

| Energy term	Assignment	Interaction Fragments
		$Rh_8^+ + 4H_2O$
ΔE_{int}		-42.55
ΔE_{elstat}		**-95.00 (23.75 per water)**
ΔE_{pauli}		113.12
ΔE_{disp}		-8.67
ΔE_{orb}		-52.00
$\Delta E_{orb(1)[\alpha]}$	$4H_2O$ (HOMO)→Rh_8^+ (LUMO) donation	-13.38 (25.7%)
$\Delta E_{orb(1)[\beta]}$	**Rh_8^+ (HOMO-1)→$4H_2O$ back-donation**	**-9.23 (17.8%)**
$\Delta E_{orb(2)[\alpha]}$	$4H_2O$ (HOMO-1)→Rh_8^+ donation	-5.79 (11.1%)
$\Delta E_{orb(2)[\beta]}$	$4H_2O$ (HOMO-1)→Rh_8^+ (LUMO+1) donation	-4.95 (9.5%)
$\Delta E_{orb(3)[\beta]}$	$4H_2O$ (HOMO)→Rh_8^+ (LUMO+4) donation	-4.38 (8.4%)
$\Delta E_{orb(4)[\beta]}$	$4H_2O$ (HOMO)→Rh_8^+ (LUMO) donation	-2.57 (4.9%)
$\Delta E_{orb(rest)[\alpha + \beta]}$		-11.66 (22.4%)

S11. NPA charge distribution
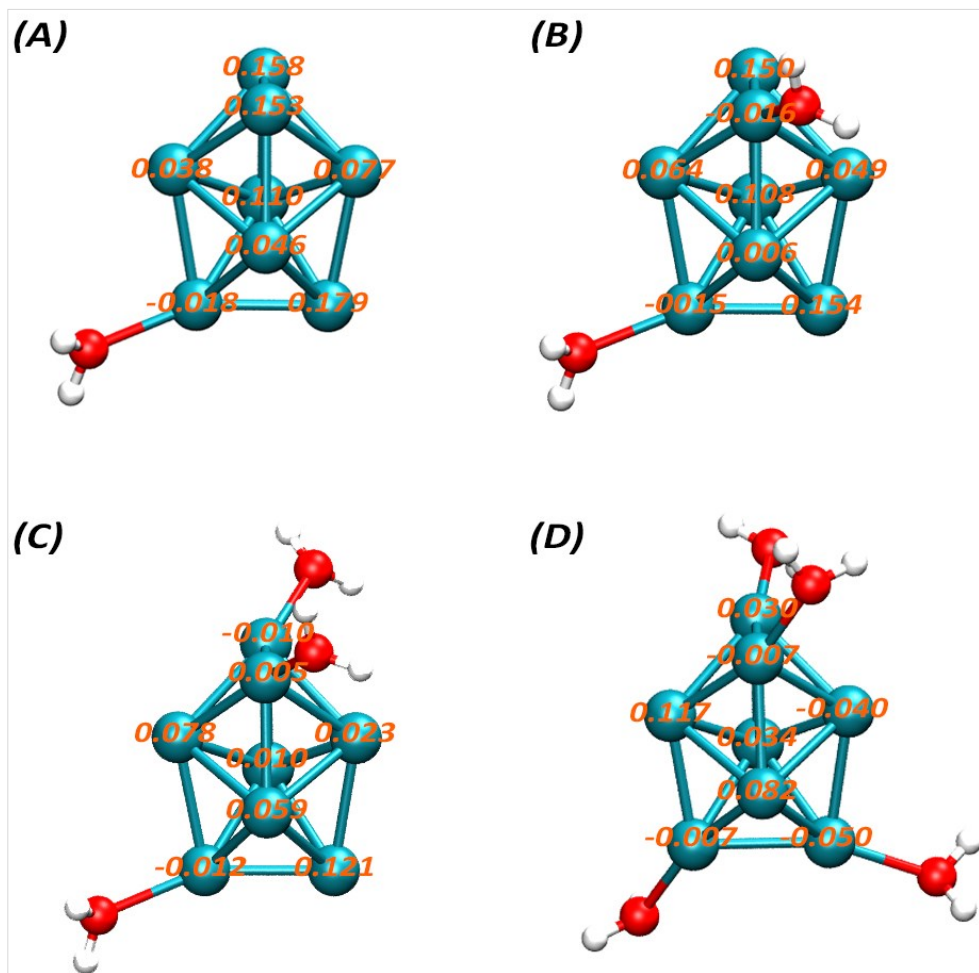
Figure S19. Surface charge distribution of $Rh_8^+(H_2O)_m$ clusters (m=1-4) obtained via natural population analysis (NPA) at B3LYP-D3/SDD level of theory for element Rh and B3LYP-D3/6-311G** for elements (O, H) (eV).

Table S14. The calculated net charges and surface electrostatic potential of atoms in Rh_8^+ cluster at the B3LYP-D3/SDD level of theory.

Rh_8^+(Atom#)	NPA	ADCH	ESP
1	**0.136**	**0.1754**	**46.0735**
2	0.108	0.0752	18.4586
3	0.108	0.0751	18.5314
4	**0.136**	**0.1753**	**46.2928**
5	0.094	0.0747	18.5407
6	0.094	0.0748	18.4144
7	**0.162**	**0.1753**	**46.1065**
8	**0.162**	**0.1753**	**46.2245**

Table S15. The calculated net charges and surface electrostatic potential of atoms in Rh_9^+ cluster at the B3LYP-D3/SDD level of theory.

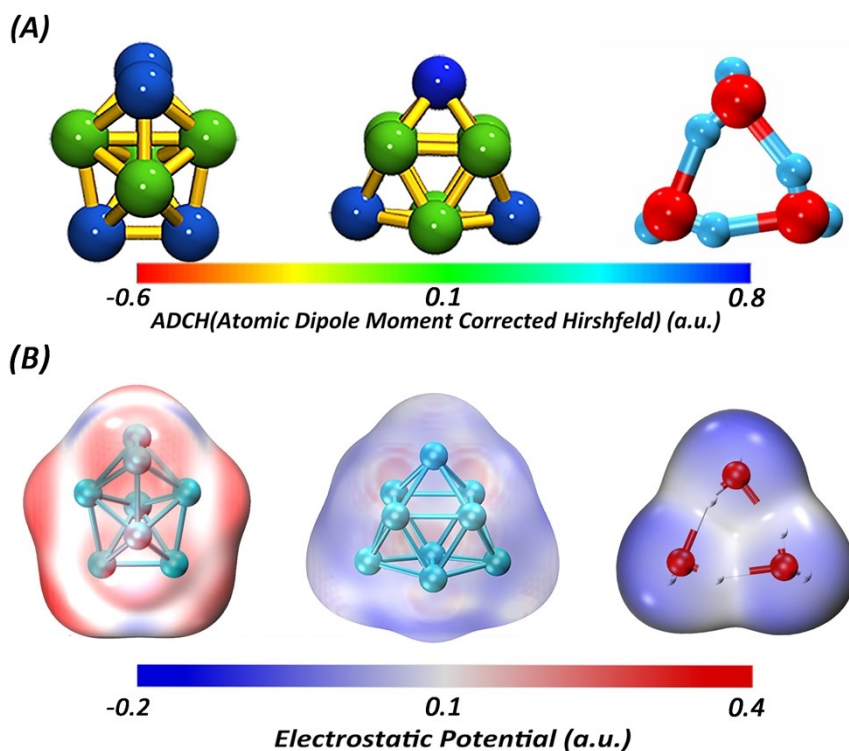| Rh_9^+(Atom#)	NPA	ADCH	ESP
1	0.086	0.0768	23.2189
2	0.076	0.0748	25.7608
3	0.076	0.0746	25.9194
4	0.087	0.0770	23.3652
5	0.076	0.0746	25.8464
6	0.076	0.0748	25.8568
7	**0.148**	**0.1769**	**21.6875**
8	**0.228**	**0.1945**	**10.1172**
9	**0.148**	**0.1769**	**21.7362**

S12. Electrostatic surface potentials (ESP)

Figure S20. (A) Atomic dipole moment corrected Hirshfeld population (ADCH) and (B) electrostatic potential analysis for $Rh_9^+(H_2O)_3$, $Rh_8^+(H_2O)_4$ and $(H_2O)_3$ cluster. The color used is according to the RGB and BWR scheme at an electron density range of $-0.6 – 0.8$ (A) and $-0.2 – 0.4$ (B), respectively.

The electrostatic surface potential (ESP) analysis [35] for Rh_8^+ and Rh_9^+ is shown in Fig. 4A and Figure S20. ESP plays a remarkable role in understanding the noncovalent interactions. Typically, there are two kinds of noncovalent bonding modes defined by ESP, "σ-hole" and "π-hole" [36-37]. On this basis, the bonding of Rh_9^+ and $(H_2O)_3$ could be rationalized by "lone pair→delocalized hole" interaction which can be regarded as a kind of super-noncovalent bonding as its long-range interactions in terms of the metal cluster and water trimer.

S13. Natural bond orbital (NBO) analysis

For NBO analysis, the second-order perturbative energy $E_{ij*}^{(2)}$ is defined as

$$E^{(2)} = q_i \frac{F_{ij}^2}{\varepsilon_i - \varepsilon_j}$$

(3)

where ε_i and ε_j are orbital energy, and F_{ij}^2 is the off-diagonal NBO Fock matrix element, and q_i represents the occupancy of donor orbital. $E_{ij*}^{(2)}$ provides a measure of the overlap interactions between the orbital i of the acceptor and the antibonding orbital j^* of the donor.
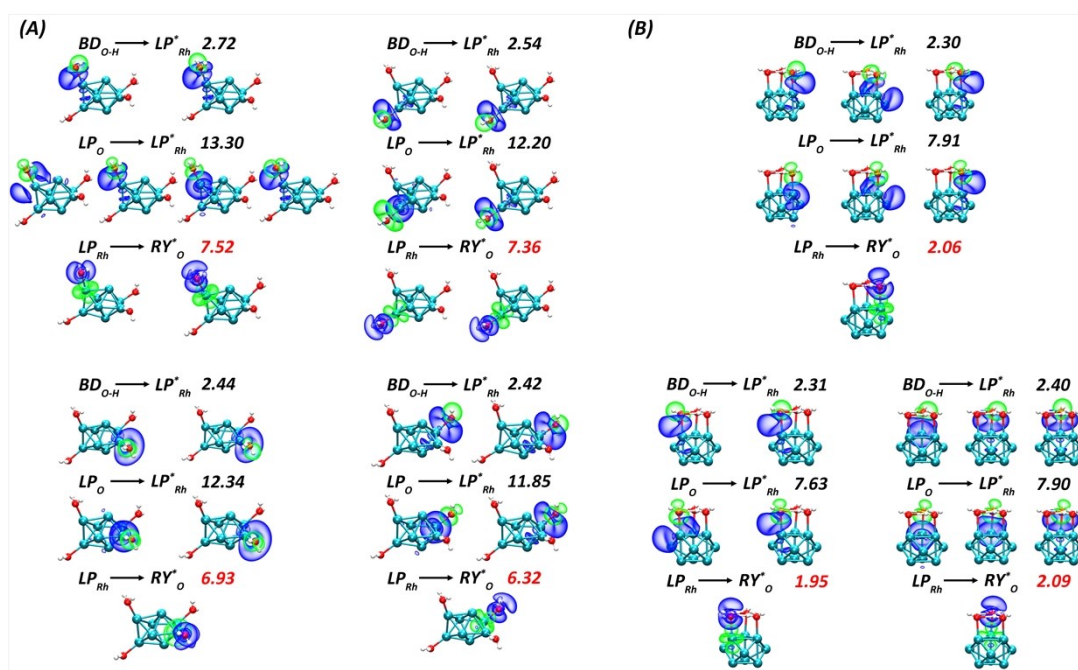

Figure S21. NBO orbital overlap and the dominant charge-transfer interactions of **(A)** $Rh_8^+(H_2O)_4$ and **(B)** $Rh_9^+(H_2O)_3$ where the unit of charge-transfer energy is Kcal/mol. The label "BD" is abbreviated for 2-center bond, "CR" for 1-center core pair, "LP" for 1-center valence lone pair, "RY*" for 1-center Rydberg, and "BD*" for 2-center anti-bond; the unstarred and starred labels corresponding to Lewis and non-Lewis NBOs, respectively.

S14. Charge decomposition analysis (CDA)

To further dissect the orbital interactions in terms of fragments bonding modes, we have carried out a charge decomposition analysis (CDA), as shown in Figure S22. For $Rh_8^+(H_2O)_4$, Rh_8^+ contributes to a major of the frontier orbitals, while the orbital of H_2O molecules only contributes with a minor amount (c.a., 2.2% and 1.2%) to the LUMO of $Rh_8^+(H_2O)_4$, resulting in a 0.3 eV increment of the HOMO-LUMO gap. Because of the unique noncovalent interaction in $Rh_9^+(H_2O)_3$, the frontier orbital of $(H_2O)_3$ shows a higher contribution (6.0%) resulting in a relatively stronger promotion of the HOMO-LUMO gap (c.a., 0.6 eV). It is worth mentioning that, for $Rh_9^+(H_2O)_6$ the unoccupied orbital of the fragment $2(H_2O)_3$ contribute about 20% to the LUMO (Figure S22C.), and a 0.94 eV increase of the H-L gap is related to the enhanced stability of Rh_9^+ under the water trimer protection.
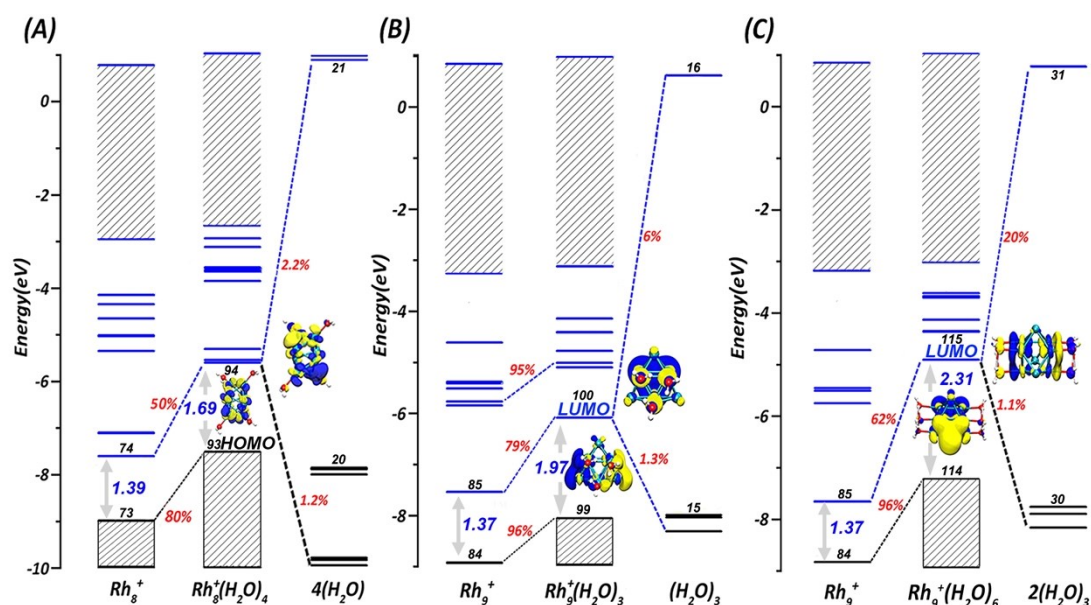

Figure S22. Molecular orbital interaction diagram of (A) $Rh_8^+(H_2O)_4$, (B) $Rh_9^+(H_2O)_3$, and (C) $Rh_9^+(H_2O)_6$ based on the charge decomposition analysis (CDA) method at B3LYP-D3/SDD for Rh, 6-311G** for O and H level. Dash lines indicate that the orbitals of two fragments contribute together to the complex orbitals with the insets showing the frontier molecular orbital of both complexes and fragments.
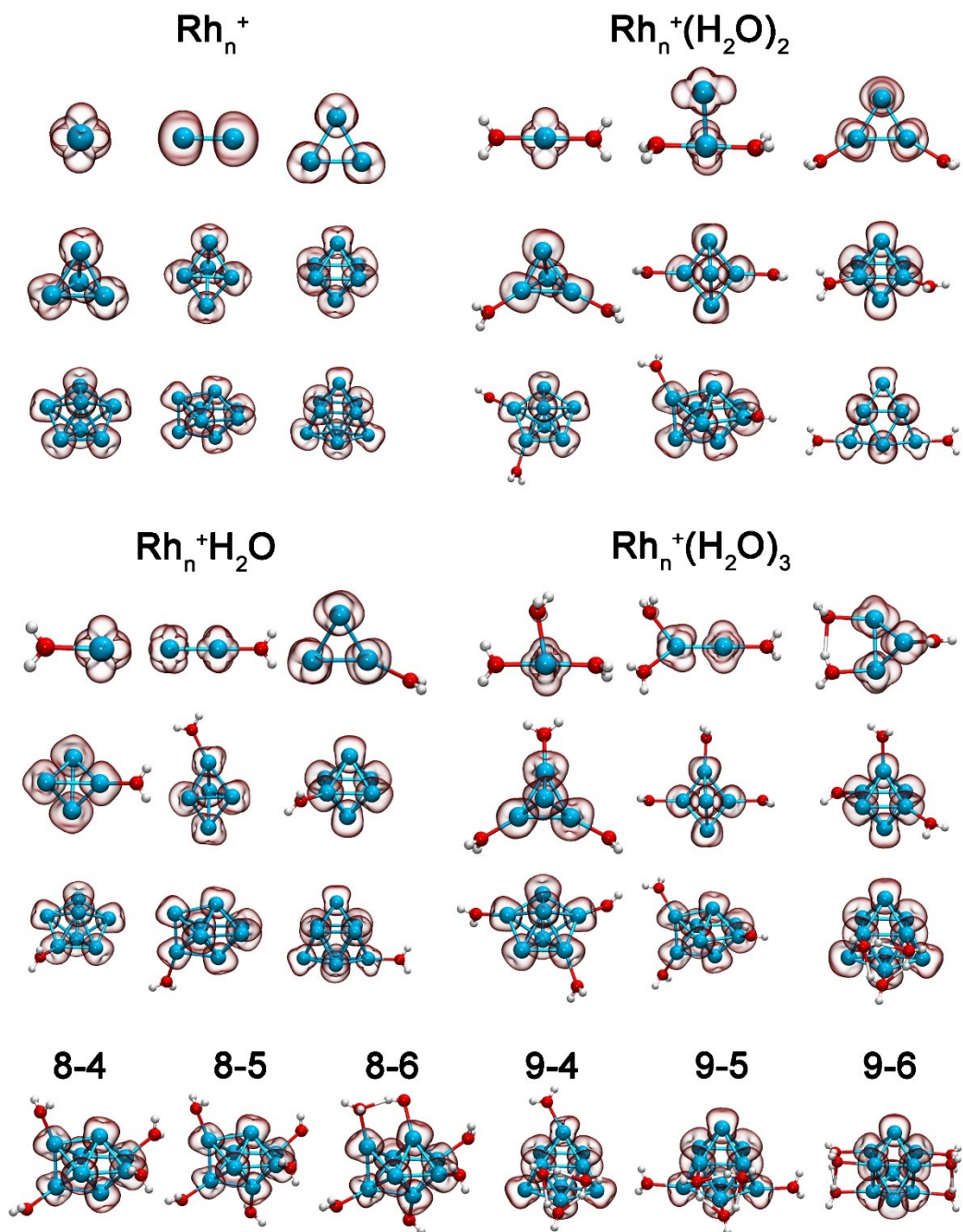
S15. Spin population

Rh$_n^+$

Rh$_n^+$(H$_2$O)$_2$

Rh$_n^+$H$_2$O

Rh$_n^+$(H$_2$O)$_3$

8-4   **8-5**   **8-6**   **9-4**   **9-5**   **9-6**

Figure S23. Spin population of Rh$_n^+$, Rh$_n^+$(H$_2$O)$_m$ (n=1-9, m=1-4) and Rh$_{8,9}^+$(H$_2$O)$_m$ (m=4-6).
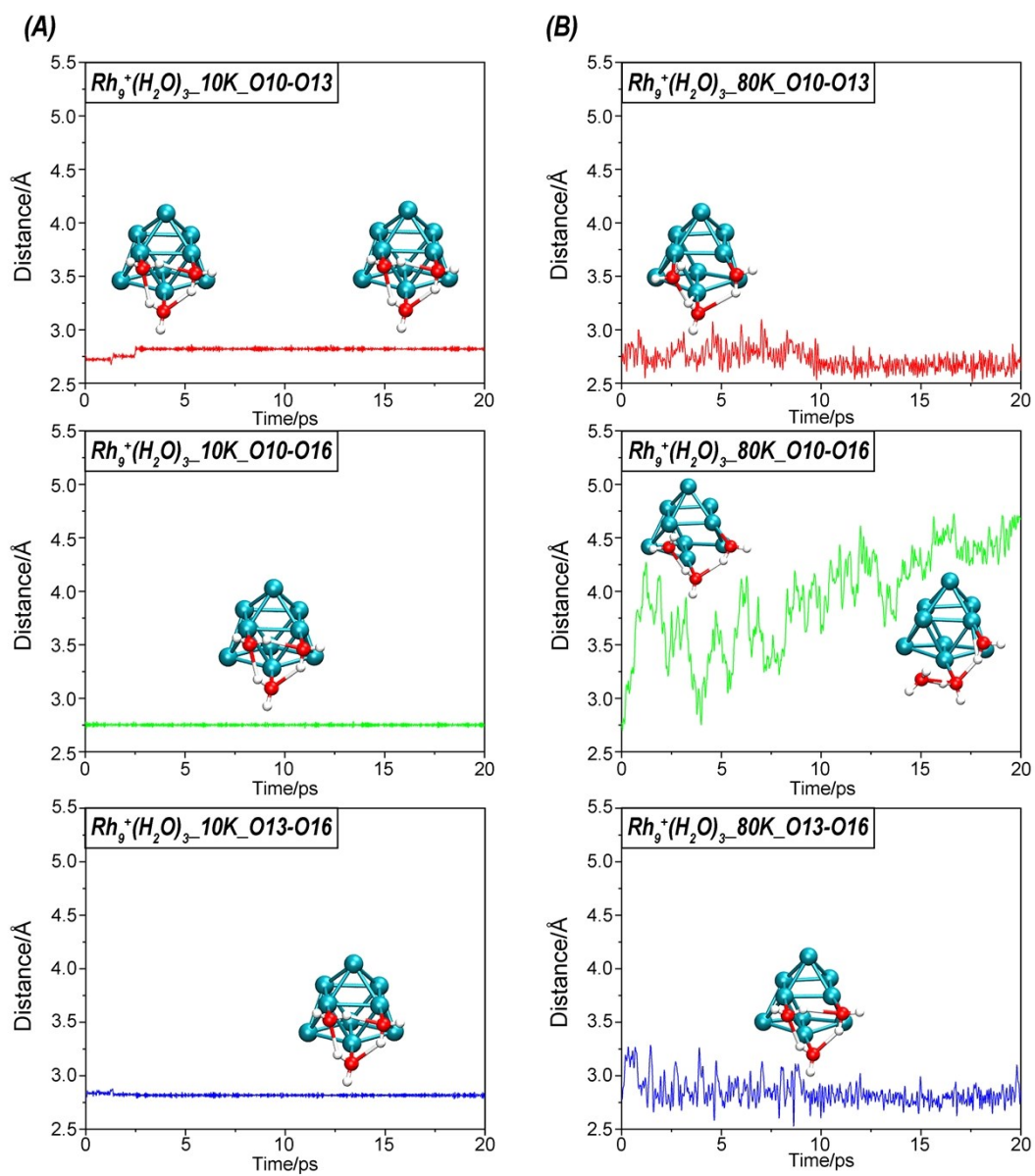
S16. Molecular dynamics (MD) simulation

Figure S24. Molecular dynamics simulation showing the bond lengths of O-O in $Rh_9^+(H_2O)_3$ cluster under 10 K and 80 K.
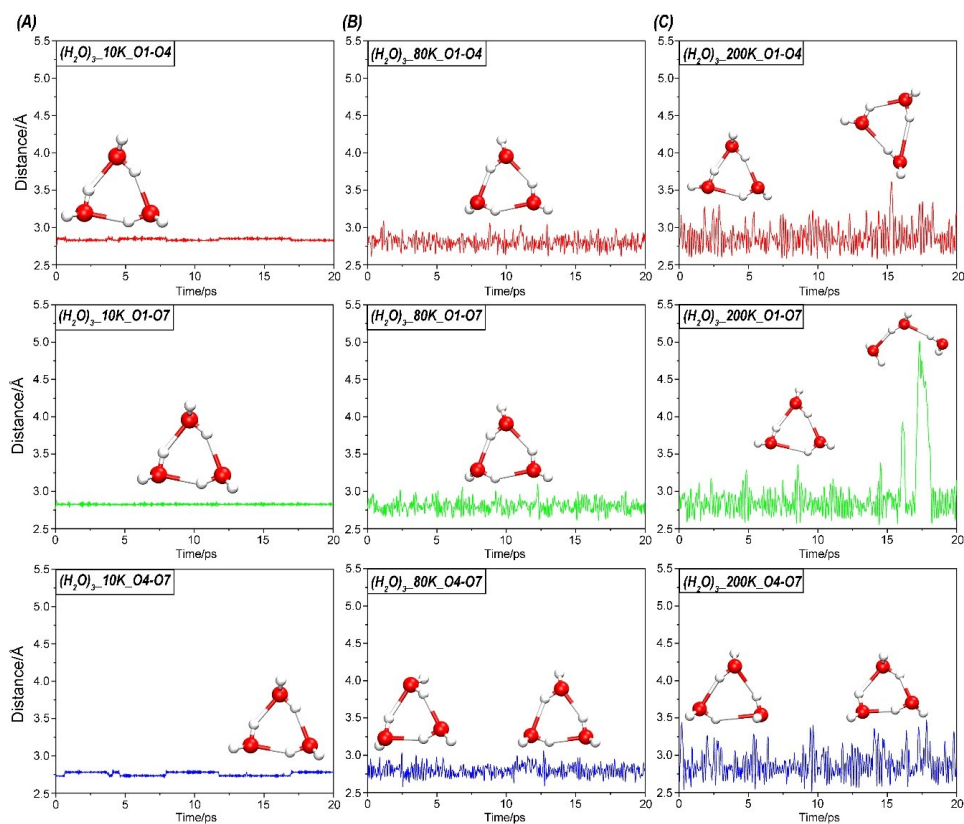
Figure S25. Molecular dynamics simulation showing the bond lengths of O-O in $(H_2O)_3$ cluster under 10 K, 80 K and 200 K.

Born-Oppenheimer molecular dynamics (BOMD) simulations were performed on $(H_2O)_3$ and $Rh_9(H_2O)_3^+$ for 20 ps at 10, 80 and 200 K, using the CP2K software package [38] with the time step of 10 fs at the PBE/DZVP level, starting from the equilibrium GM geometry with random velocities assigned to the atoms. The initial conditions were chosen to correspond to a microcanonical ensemble [39-40]. The actual temperature of the system was found to be close to the initial setup during the simulation.

References

(1)   Zhang, H.; Wu, H.; Jia, Y.; Geng, L.; Luo, Z.; Fu, H.; Yao, J., An integrated instrument of DUV-IR photoionization mass spectrometry and spectroscopy for neutral clusters. *Rev. Sci. Instrum.* **2019,** *90* (7), 073101.

(2)   Becke, A. D., Density-functional thermochemistry. III. The role of exact exchange. *J. Chem. Phys.* **1993,** *98* (7), 5648-5652.

(3)   Lee, C.; Yang, W.; Parr, R. G., Development of the Colle-Salvetti correlation-energy formula into a functional of the electron density. *Phys. Rev. B Condens Matter* **1988,** *37* (2), 785-789.

(4)   Frisch, M. J.; Trucks, G. W.; Schlegel, H. B.; Scuseria, G. E.; Robb, M. A.; Cheeseman, J. R.; Scalmani, G.; Barone, V.; Mennucci, B.; Petersson, G. A.; Nakatsuji, H.; Caricato, M.; Li, X.; Hratchian, H. P.; Izmaylov, A. F.; Bloino, J.; Zheng, G.; Sonnenberg, J. L.; Hada, M.; Ehara, M.; Toyota, K.; Fukuda, R.; Hasegawa, J.; Ishida, M.; Nakajima, T.; Honda, Y.; Kitao, O.; Nakai, H.; Vreven, T.; Montgomery, J. A.; Peralta, J. E.; Ogliaro, F.; Bearpark, M.; Heyd, J. J.; Brothers, E.; Kudin, K. N.; Staroverov, V. N.; Kobayashi, R.; Normand, J.; Raghavachari, K.; Rendell, A.; Burant, J. C.; Iyengar, S. S.; Tomasi, J.; Cossi, M.; Rega, N.; Millam, J. M.; Klene, M.; Knox, J. E.; Cross, J. B.; Bakken, V.; Adamo, C.; Jaramillo, J.; Gomperts, R.; Stratmann, R. E.; Yazyev, O.; Austin, A. J.; Cammi, R.; Pomelli, C.; Ochterski, J. W.; Martin, R. L.; Morokuma, K.; Zakrzewski, V. G.; Voth, G. A.; Salvador, P.; Dannenberg, J. J.; Dapprich, S.; Daniels, A. D.; Farkas; Foresman, J. B.; Ortiz, J. V.; Cioslowski, J.; Fox, D. J. *Gaussian 09 Rev. E.01*, Gaussian 09 Rev. E.01, Wallingford CT, 2009.

(5)   Andrae, D.; HauBermann, U.; Dolg, M.; Stoll, H.; PreuB, H., Energy-adjusted ab initio pseudopotentials for the second and third row transition elements. *Theor. Chim. Acta.* **1990,** *77*, 121-141.

(6)   Hehre, W. J.; Ditchfield, R.; Pople, J. A., Self-consistent molecular orbital methods. XII. Further extensions of gaussian—type basis sets for use in molecular orbital studies of organic molecules. *J. Chem. Phys.* **1972,** *56* (5), 2257-2261.

(7)   Ditchfield, R.; Hehre, W. J.; Pople, J. A., Self-Consistent Molecular-Orbital Methods. IX. An Extended Gaussian-Type Basis for Molecular-Orbital Studies of Organic Molecules. *J. Chem. Phys.* **1971,** *54*, 724.

(8)   Brathwaite, A. D.; Abbott-Lyon, H. L.; Duncan, M. A., Distinctive Coordination of CO vs N_2 to Rhodium Cations: An Infrared and Computational Study. *J. Phys. Chem. A* **2016,** *120* (39), 7659-7670.

(9)   Su, B.-F.; Fu, H.-Q.; Yang, H.-Q.; Hu, C.-W., Catalytic reduction of NO by CO on Rh4+ clusters: a density functional theory study. *Catal. Sci. Technol.* **2015,** *5* (6), 3203-3215.

(10) Yang, H. Q.; Fu, H. Q.; Su, B. F.; Xiang, B.; Xu, Q. Q.; Hu, C. W., Theoretical Study on the Catalytic Reduction Mechanism of NO by CO on Tetrahedral Rh4 Subnanocluster. *J. Phys. Chem. A* **2015,** *119* (47), 11548-64.

(11) Beltrán, M. R.; Buendía Zamudio, F.; Chauhan, V.; Sen, P.; Wang, H.; Ko, Y. J.; Bowen, K., Ab initio and anion photoelectron studies of Rhn (n = 1 − 9) clusters. *Eur. Phys. J. D* **2013,** *67* (3).

(12) Dutta, A.; Mondal, P., Structural evolution, electronic and magnetic manners of small rhodium $Rh_n^{+/-}$ (n = 2–8) clusters: a detailed density functional theory study. *RSC Adv.* **2016,** *6* (9), 6946-6959.

(13) Nagata, T.; Kudoh, S.; Miyajima, K.; Bakker, J. M.; Mafuné, F., Adsorption of Multiple NO Molecules on Rhn+ (n = 6, 7) Investigated by Infrared Multiple Photon Dissociation Spectroscopy. *J. Phys. Chem. C* **2018,** *122* (40), 22884-22891.

(14) Koyama, K.; Nagata, T.; Kudoh, S.; Miyajima, K.; Huitema, D. M.; Chernyy, V.; Bakker, J. M.; Mafune, F., Geometrical structures of partially oxidized rhodium cluster cations, $Rh_6O_m^+$ (m = 4, 5,

6), revealed by infrared multiple photon dissociation spectroscopy. *J. Phys. Chem. A* **2016,** *120* (43), 8599-8605.

(15) Mafuné, F.; Koyama, K.; Nagata, T.; Kudoh, S.; Yasuike, T.; Miyajima, K.; Huitema, D. M. M.; Chernyy, V.; Bakker, J. M., Structures of rhodium oxide cluster cations $Rh_7O_m^+$ (m = 4–7, 12, 14) revealed by infrared multiple photon dissociation spectroscopy. *J. Phys. Chem. C* **2019,** *123* (10), 5964-5971.

(16) Xu, Q.-Q.; Yang, H.-Q.; Gao, C.; Hu, C.-W., Theoretical study on the reaction mechanism of NO and CO catalyzed by Rh atom. *Struct. Chem.* **2012,** *24* (1), 13-23.

(17) Kresse, G.; Furthmuller, J., Efficient iterative schemes for ab initio total-energy calculations using a plane-wave basis set. *Phys. Rev. B* **1996,** *54* (16), 11169-11186.

(18) Kresse, G.; Joubert, D., From ultrasoft pseudopotentials to the projector augmented-wave method. *Phys. Rev. B* **1999,** *59* (3), 1758-1775.

(19) Grimme, S.; Ehrlich, S.; Goerigk, L., Effect of the damping function in dispersion corrected density functional theory. *J. Comput. Chem.* **2011,** *32* (7), 1456-1465.

(20) Goerigk, L.; Hansen, A.; Bauer, C.; Ehrlich, S.; Najibi, A.; Grimme, S., A look at the density functional theory zoo with the advanced GMTKN55 database for general main group thermochemistry, kinetics and noncovalent interactions. *Phys. Chem. Chem. Phys.* **2017,** *19* (48), 32184-32215.

(21) Bader, R. F. W., Atoms in Molecules. *Acc. Chem. Res.* **1985,** *18*, 9-15.

(22) Schmider, H. L.; Becke, A. D., Chemical content of the kinetic energy density. *J. Mol. Struc.-THEOCHEM* **2000,** *527* (1), 51-61.

(23) Johnson, E. R.; Keinan, S.; Mori-Sánchez, P.; Contreras-García, J.; Cohen, A. J.; Yang, W., Revealing noncovalent interactions. *J. Am. Chem. Soc.* **2010,** *132* (18), 6498-6506.

(24) Weinhold, F.; Landis, C., *Valency and Bonding: A Natural Bond Orbital Donor-Acceptor Perspective*. Cambridge University Press: Cambridge, 2005.

(25) E. D. Glendening, J. K. B., A.E. Reed, J. E. Carpenter, J. A. Bohmann, C.M. Morales, C. R. Landis, and F. Weinhold *NBO 6.0.*, Theoretical Chemistry Institute, University of Wisconsin, Madison, 2.13.

(26) Fu, L.; Han, H.-L.; Lee, Y.-P., Infrared absorption of methanethiol clusters $(CH_3SH)_n$, n=2-5, recorded with a time-of-flight mass spectrometer using IR depletion and VUV ionization. *J. Chem. Phys.* **2012,** *137* (23).

(27) Humphrey, W.; Dalke, A.; Schulten, K., VMD: Visual Molecular Dynamics. *J Mol Graph Model* **1996,** *14*, 33-38.

(28) Dapprich, S.; Frenking, G., Investigation of Donor-Acceptor Interactions: A Charge Decomposition Analysis Using Fragment Molecular Orbitals. *J. Phys. Chem.* **1995,** *99* (23), 9352-9362.

(29) Murray, J. S.; Lane, P.; Clark, T.; Riley, K. E.; Politzer, P., Sigma-holes, pi-holes and electrostatically-driven interactions. *J. Mol. Model.* **2012,** *18* (2), 541-8.

(30) R.D., C.; T.L., B., *Encyclopedia of computational chemistry*. Wiley: New York, 1998; Vol. 3, p 2086.

(31) Politzer, P.; Murray, J. S., The fundamental nature and role of the electrostatic potential in atoms and molecules. *Theor. Chem. Acc.* **2002,** *108* (3), 134-142.

(32) Cremer, D.; Kraka, E., Chemical Bonds without Bonding Electron Density — Does the Difference Electron-Density Analysis Suffice for a Description of the Chemical Bond? *Angew. Chem. Int. Ed.* **1984,** *23* (8), 627-628.

(33) Espinosa, E.; Alkorta, I.; Elguero, J.; Molins, E., From weak to strong interactions: A

comprehensive analysis of the topological and energetic properties of the electron density distribution involving X–H···F–Y systems. *J. Chem. Phys.* **2002,** *117* (12), 5529-5542.

(34) Schmidt, M. W.; Baldridge, K. K.; Boatz, J. A.; Elbert, S. T.; Gordon, M. S.; Jensen, J. H.; Koseki, S.; Matsunaga, N.; Nguyen, K. A.; Su, S.; Windus, T. L.; Dupuis, M.; Montgomery Jr, J. A., General atomic and molecular electronic structure system. *J. Comput. Chem.* **1993,** *14* (11), 1347-1363.

(35) Murray, J. S.; Politzer, P., The electrostatic potential: an overview. *WIREs Comput. Mol. Sci.* **2011,** *1* (2), 153-163.

(36) Politzer, P.; Murray, J. S., sigma-holes and pi-holes: Similarities and differences. *J. Comput. Chem.* **2018,** *39* (9), 464-471.

(37) Murray, J. S.; Politzer, P., Molecular electrostatic potentials and noncovalent interactions. *WIREs Comput. Mol. Sci.* **2017,** *7* (6).

(38) VandeVondele, J.; Krack, M.; Mohamed, F.; Parrinello, M.; Chassaing, T.; Hutter, J., Quickstep: Fast and accurate density functional calculations using a mixed Gaussian and plane waves approach. *Comput. Phys. Commun.* **2005,** *167* (2), 103-128.

(39) Li, X.; Millam, J. M.; Schlegel, H. B., Glyoxal photodissociation. II. An ab initio direct classical trajectory study of $C_2H_2O_2 \rightarrow CO+H_2CO$. *J. Chem. Phys.* **2001,** *115* (15), 6907-6912.

(40) Li, X.; Millam, J. M.; Schlegel, H. B., Glyoxal photodissociation. An ab initio direct classical trajectory study of $C_2H_2O_2 \rightarrow H_2+2\,CO$. *J. Chem. Phys.* **2001,** *114* (20), 8897-8904.